
**UNIVERSIDADE FEDERAL DO RIO DE JANEIRO**

**INSTITUTO DE FÍSICA**

# Dynamical Casimir Effects with Atoms and Spinning Nanoparticles

**Guilherme Costa Matos**

Tese de Doutorado apresentada ao Programa de Pós-Graduação em Física do Instituto de Física da Universidade Federal do Rio de Janeiro - UFRJ, como parte dos requisitos necessários à obtenção do título de Doutor em Ciências (Física).

**Orientador: Paulo Américo Maia Neto**

**Coorientador: François Michel Claude Impens**

**Rio de Janeiro**

**Dezembro de 2025**

Dynamical Casimir Effects with Atoms and Spinning Nanoparticles

**Guilherme Costa Matos**

Paulo Américo Maia Neto
François Michel Claude Impens

Tese de Doutorado submetida ao Programa de Pós-Graduação em Física, Instituto de Física, da Universidade Federal do Rio de Janeiro – UFRJ, como parte dos requisitos necessários à obtenção do título de Doutor em Ciências (Física).

Aprovada por:

.....
Prof. Dr. Paulo Américo Maia Neto, IF-UFRJ
(Presidente e Orientador)

.....
Prof. Dr. François Michel Claude Impens, IF-UFRJ
(Coorientador)

.....
Prof. Dr. Felipe Siqueira de Souza da Rosa, IF-UFRJ

.....
Prof. Dr. Thiago Barbosa dos Santos Guerreiro, PUC-Rio

.....
Prof. Dr. Felipe Arruda de Araújo Pinheiro, IF-UFRJ

.....
Prof. Dr. Fernando da Rocha Vaz Bandeira de Melo, CBPF

.....
Prof. Dr. Carlos Augusto Domingues Zarro, IF-UFRJ

Rio de Janeiro, RJ – Brasil
18 de Dezembro de 2025

M381d Matos, Guilherme Costa

Dynamical Casimir Effects with Atoms and Spinning Nanoparticles / Guilherme Costa Matos - Rio de Janeiro: UFRJ/IF, 2025.

93f.

Orientador: Paulo Américo Maia Neto

Coorientador: François Michel Claude Impens

Tese (doutorado) - UFRJ / Instituto de Física / Programa de Pós-graduação em Física, 2025.

1. Efeito Casimir dinâmico. 2. Nanopartículas girantes. 3. Vácuo quântico. 4. Efeito Sagnac. 5. Emissão de fótons. I. Neto, Paulo Américo Maia, orient. II. Impens, François Michel Claude, coorient. III. Dynamical Casimir Effects with Atoms and Spinning Nanoparticles.

*We are not sufficiently astonished by the fact that any science may be possible, that is, that our reason should provide us with the means of understanding at least certain aspects of what happens around us in nature.*

— Louis de Broglie

*Para Ana Cristina.*

# Resumo

## Dynamical Casimir Effects with Atoms and Spinning Nanoparticles

**Guilherme Costa Matos**

**Orientador: Paulo Américo Maia Neto**

**Coorientador: François Claude Michel Impens**

Resumo da Tese de Doutorado apresentada ao Programa de Pós-Graduação em Física do Instituto de Física da Universidade Federal do Rio de Janeiro - UFRJ, como parte dos requisitos necessários à obtenção do título de Doutor em Ciências (Física).

Motivada por experiências recentes com nanopartículas levitadas e em rotação ultrarrápida, esta tese apresenta novos efeitos na interação de partículas em rotação com o vácuo quântico. A primeira parte da tese estuda o análogo da eletrodinâmica quântica do efeito Sagnac, no qual a rotação de uma partícula neutra nas proximidades de um interferômetro atômico induz uma fase nas ondas de matéria propagantes. A fase resultante é uma fase de Berry geométrica proporcional à velocidade angular da partícula. Uma rotação confinada a uma região do espaço, deixando um traço de não inercialidade em um referencial inercial, sugere uma analogia com o efeito Aharonov-Bohm. Levando em conta as ressonâncias plasmônicas da partícula, a análise revela que a magnitude da fase está próxima do limite de medição dos interferômetros atômicos de última geração. A força exercida sobre um átomo por uma partícula em rotação também é calculada e monstra-se ser análoga à força de Coriolis. A segunda parte da tese examina a emissão de fótons por uma partícula neutra não esférica em rotação. Desde que o eixo de rotação seja ortogonal

ao eixo de simetria da partícula, a interação da partícula com o campo produz bandas laterais de frequência para o campo espalhado, levando à emissão de pares de fótons pelo efeito Casimir dinãmico. A taxa de emissão de fótons é obtida para esferóides metálicos e dielétricos e é aumentada quando a frequência de rotação está próxima de uma ressonância plasmônica ou polaritônica. A fim de otimizar a taxa de emissão, a velocidade da ponta da partícula é fixada e a dependência com a geometria é analisada.

**Palavras-chave:** 1. Efeito Casimir dinâmico. 2. Nanopartículas girantes. 3. Vácuo quântico. 4. Efeito Sagnac. 5. Emissão de fótons.

# Abstract

## Dynamical Casimir Effects with Atoms and Spinning Nanoparticles

**Guilherme Costa Matos**

**Orientador: Paulo Américo Maia Neto**

**Coorientador: François Claude Michel Impens**

*Abstract* da Tese de Doutorado apresentada ao Programa de Pós-Graduação em Física do Instituto de Física da Universidade Federal do Rio de Janeiro - UFRJ, como parte dos requisitos necessários à obtenção do título de Doutor em Ciências (Física).

Motivated by recent experiments with levitated, ultra-fast rotating nanoparticles, this thesis presents new effects in the interaction of spinning particles with the quantum vacuum. The first part of the thesis studies the quantum electrodynamical analog of the Sagnac effect, in which the rotation of a neutral particle in the vicinity of an atom interferometer induces a phase on the propagating matter waves. The resulting phase is a geometric Berry phase proportional to the angular velocity of the particle. A rotation confined to a region of space leaving a trace of non-inertiality in an inertial frame suggests an analogy with the Aharonov-Bohm effect. Taking the particle's plasmon resonances account, the analysis reveals that the phase magnitude is close to the limit of measurement for current state of the art atom interferometers. The force on an atom by a rotating particle is also calculated, and is shown to be analogous to the Coriolis force. The second part of the thesis deals with the photon emission by a rotating non-spherical neutral particle. Provided that the rotation axis is orthogonal to particle symmetry axis, the interaction

of the particle with the field produces frequency sidebands of the scattered field, leading to the emission of dynamical Casimir photon pairs. The photon emission rate is obtained for metallic and dielectric spheroids and is enhanced when the rotation frequency is near a plasmonic or polaritonic resonance. In order to optimize the emission rate, the velocity of the particle's tip is fixed and the dependence with the particle's geometry is considered.

**Keywords:** 1. Dynamical Casimir effect. 2. Rotating nanoparticles. 3. Quantum vacuum. 4. Sagnac effect. 5. Photon emission.

# List of Publications

1. **G. C. Matos**, R. d. M. e. Souza, P. A. M. Neto, and F. Impens, "Quantum vacuum sagnac effect", Physical Review Letters, vol. 127, no. 27, p. 270401, 2021

2. F. Impens, R. d. M. e Souza, **G. C. Matos**, and P. A. M. Neto, "Dynamical casimir effects with atoms: From the emission of photon pairs to geometric phases", Europhysics Letters, vol. 138, no. 3, p. 30001, 2022.

3. L. Alonso, **G. C. Matos**, F. Impens, P. A. Maia Neto, and R. de Melo e Souza, "Multipole approach to the dynamical casimir effect with finite-size scatterers," Entropy, vol. 26, no. 3, p. 251, 2024.

4. **G. C. Matos**, L. Bianchi, J. N. Munday, F. Impens, R. de Melo e Souza, and P. A. Maia Neto,"Dynamical casimir photons from rotation of a nonspherical particle," in preparation.

# Agradecimentos

A Deus, por absolutamente tudo.

Aos meus orientadores, Prof. Paulo Américo e Prof. François Impens, por todo o aprendizado e trabalho exemplar de orientação durante os anos de mestrado e doutorado. As ideias e discussões que me apresentaram têm um peso inestimável para minha formação.

Ao Prof. Reinaldo de Melo, cuja colaboração foi fundamental para os trabalhos apresentados nesta tese. As enriquecedoras discussões de física que tive com ele sempre me motivaram desde meu primeiro ano de graduação, assim como seus conselhos auxiliaram muito minha trajetória acadêmica.

À minha irmã, Maria Eduarda, por todo o carinho, apoio e amizade.

À Carol Vieira, pela companhia e pelo incentivo que foram fundamentais para mim durante meus anos na pós-graduação.

Aos meus pais, Joel e Maria da Paz, por terem sido sempre presentes e terem feito tudo ao seu alcance para apoiar minha formação.

A Rosane, Jorge e Caio, que prontamente me receberam em suas vidas com todo o carinho.

A Ana Cristina (in memoriam), Roberto, Luísa, João Victor e Vera Lúcia, pelo acolhimento que jamais serei capaz de retribuir.

À Kívia Rodrigues, cuja ajuda foi indispensável para a conclusão desta tese.

Ao amigo Lucas Bianchi, com quem tive a honra e o privilégio de colaborar desde sua iniciação científica. Sua participação acrescentou muito aos trabalhos apresentados aqui.

Ao prof. Celso Villas-Bôas, por propor excelentes ideias e discussões.

Aos amigos Arthur Luna, Bruno Magacho, Lucca Martins, Gabriel Picanço, Larissa Inácio, Marcus Prado, Patrícia Andrade, Anselmo Pontes e Theo Saback, pelo privilégio de suas companhias que tanto alegraram meus anos na UFRJ.

Aos amigos Felipe Vieira, Guilherme Theodoro, Pedro Zanardi, Rafael Machado, João Braga, Leonardo Cármine, Gabriel Krull, Lucas Avelino e Matheus "Lutador" Martins, que me acompanharam durante boa parte da minha vida.

Aos professores Carlos Farina e Carlos Zarro, que, além de excelentes cursos, me deram valiosos conselhos ao longo da minha formação.

Ao prof. Maurício Hippert, por ter me ajudado bastante a iniciar minha trajetória na física.

Aos amigos Ademir, Jenílson, Luiz Gonzaga, Luiz Felipe, Nathan, Marcos Jorge "MJ", Marcos Vinícius "MV", Nathan, Vagner, Júlio Vieira, Júlio César, Enrick, Luiz Flavio, Fernando Henriques, Rodrigo e Rafael Alves, por todo o apoio.

Aos funcionários da secretaria de pós-graduação, Igor e Luiza, que sempre foram extremamente solícitos e sempre resolveram qualquer problema com rapidez.

Por fim, gostaria de agradecer à CAPES pelo apoio financeiro, imprescindível para o desenvolvimento das pesquisas desta tese.

# Contents

# List of Figures

# List of Symbols

$[A, B]$ Commutator of operators $A$ and $B$

$\alpha_0^A$ Static atomic polarizability

$\mathbf{d}$ Electric dipole moment operator

$\boldsymbol{\alpha}$ Polarizability tensor

$\boldsymbol{\alpha}^A$ Atomic polarizability tensor

$\mathbf{r}_A$ Atomic position operator

$\delta(x)$ Dirac delta distribution

$\delta_{lm}$ Kronecker delta

$\mathbf{E}$ Electric field operator

$\epsilon$ Dielectric function

$\epsilon_0$ Vacuum permittivity

$\hat{\mathbf{v}}$ Unitary vector

$\hbar$ Reduced Planck constant

$\mathbb{1}$ Identity matrix

$\boldsymbol{\Omega}$ Angular velocity vector

$\mathbf{G}^R$ Retarded Green function

$\mathscr{J}_j(x)$ Spherical Bessel function of the first kind

$\omega$ Angular frequency

$\phi$ Interferometric phase

$\psi$ Wavefunction

$\rho$ Density matrix

$\mathbf{r}$ Position vector

$\tilde{A}$ Operator $A$ in the interaction picture

$\{A, B\}$ Anticommutator of operadors $A$ e $B$

$c$ Speed of light

*c.c.* Complex conjugate

$f'(x)$ Derivative of function $f(x)$

$f(\omega)$ Fourier transform of $f(t)$

$H$ Hamiltonian operator

$z^*$ Complex conjugate of $z$

i Imaginary unit

# Introduction

*"The apparent emptiness of empty space is an illusion. In fact, empty space is a multi-layered, multicolored superconductor. ... It's a highly structured, active medium, whose activity becomes visible when we probe it with sufficiently delicate instruments."*

— Frank Wilczek

One of the most shocking predictions from quantum electrodynamics is that the energy of the electromagnetic field in its zero quanta (vacuum) state is non zero. This implies the existence of quantum vacuum fluctuations. The seminal work by H. B. G. Casimir and D. Polder [3, 4] on the interaction energy between neutral objects in the vacuum brought physical reality to the effects of the quantum vacuum (see [5] for a comprehensive historical discussion). The measurement of the Casimir force by S. K. Lamoreaux [6] cemented the Casimir effect as an important research topic in physics (see [7, 8] for reviews) with recent relevant theoretical and experimental developments [9–15].

However, the same does not apply for dynamical Casimir effects, i.e. motional effects of the quantum vacuum, which have not yet been detected. That is the case for the quantum friction (QF) [1] and the dynamical Casimir effect (DCE). The QF is characterized by a dissipative velocity-dependent vacuum induced force acting on the relative motion between a polarizable particle and a surface or even between surfaces [22–32], while the Dynamical Casimir effect consists in the parametric emission of photonic pairs

[1] see [16, 17] for reviews on QF and [18–21] for the DCE

by a neutral object undergoing a non-uniform motion [33–42]. The scale of wavelength set by the accessible experimental velocities is much greater than the typical wavelengths of appreciable electromagnetic response of materials, resulting in very small effects for both QF and DCE. The smallness of these effects has not discouraged research, and extensive literature has been produced on the topics.

The last few years saw the rise of experiments with levitated fast rotating microscopic rotors [2,43–47], with a current record for the rotation frequency of 6 GHz [48]. Similar experiments have been performed to explore the boundaries between classical and quantum mechanics by cooling a trapped levitated nanoparticle to its motional ground state [49]. The high velocities motivated proposals to employ this experimental platform to measure QF [2, 44], and combined with theoretical work on QF for rotating particles [9, 50–53], could result in a direct measurement of the effect in the next few years.

Given the potential of rotating nanoparticles to probe dynamical quantum vacuum effects, the present thesis proposes new effects in the interaction of non-relativistic spinning particles with the quantum vacuum.

The thesis is organized as follows. Chapter 1 presents a review of the quantum open system approach for atom interferometers developed in Ref. [54]. The interaction of the atom with its surroundings is parametrized by the atomic center-of-mass position, and the interaction with the internal atomic degrees of freedom and with the quantum electromagnetic field gives rise to an interferometric phase and to decoherence. In second order of perturbation theory, the total phase is the sum of contributions of atomic interactions in one interferometer path and both paths simultaneously. Those contributions are regarded as local and nonlocal, respectively. The results are applied to an atom interferometer near a neutral object in the vacuum. In that case, the induced phase carries information on the motional corrected Casimir interaction between the atom and the object.

Chapter 2 employs the theory of dynamical Casimir phases of chapter 1 to derive the quantum vacuum Sagnac phase (QVSP), the phase induced on an atom interferometer

by a rotating nanoparticle in its vicinity. The phase is proportional to the rotational angular frequency, in direct analogy with the standard Sagnac effect [55]. The phase is demonstrated to be a geometric Berry phase analogous to the Aharonov-Bohm effect. As recent theoretical works proposed geometric phases to detect quantum friction interactions between atoms and surfaces [27, 29], the QVSP also represents an advance for rotational coupling with the quantum vacuum, since its magnitude for finite-width wavepackets is shown to be close to the sensitivity limit of modern atom interferomers, when the atomic transition frequency is near the nanoparticle's plasmonic resonance. The analogy with the standard Sagnac effect is deepened by considering the force on the atom by the rotating nanoparticle, as the result shows a force similar to the Coriolis force.

Chapter 3 presents the DCE for rotating nanoparticles. The photon emission rate is obtained for a non-spherical nanoparticle rotating perpendicular to its symmetry axis. The scattering of electric field by the spinning particle results in a rotational Doppler shift of field modes that produces a rotation dependent emission spectrum. The spectrum depends on the polarizability tensor of the nanoparticle, which contains information on the material and geometry. An analytical approach to the DCE emission for metallic spheroids is presented, showing that the emission peaks at plasmon resonances. The emission rate for dielectric nanoparticles is also obtained. The role of geometry is explored by fixing the linear velocity of the tip of the particle, allowing the analysis of the emission dependence with radius and eccentricity.

# Chapter 1

# Dynamical Casimir Atomic Phases

*"When it comes to atoms, language can be used only as in poetry."*

— Niels Bohr

The interaction energy between two ground-state atoms and or an atom and a plane surface, with the inclusion of the retardation effect of the electromagnetic field, was first shown by Casimir & Polder in 1948 [3]. Since then, many different systems have been used to investigate the Casimir effect with atoms, with most of them relying on the hypothesis of static atoms, given that the correction on the energies due to the non-relativistic motion is very small [23, 56].

The temporal evolution of matter waves ensures that interactions with external factors are registered in the wave function as a phase. In the context of Casimir forces on atoms, this phase would be a footprint of the interaction with another object modified by atomic propagation. Given the sensibility of atom interferometers, the measurement of the phase (henceforth referred as dynamical Casimir phase) could be an experimental approach for the detection of dynamical corrections of dispersive interactions. Moreover, experiments with atom interferometers have been performed to measure Van der Waals interactions between atoms and surfaces [57–59], with recent experiments measuring retardation corrections of the Casimir-Polder potential [60, 61]. In addition, atomic interferometers based on optical tweezers had been proposed to detect retardation effects

in the long range Casimir-Polder potential [62].

This chapter presents the derivation of the dynamical Casimir phase obtained by an atom propagating in the vicinity of an arbitrary neutral object using the open quantum system approach developed in Ref. [54], treating the evolution of a coherent superposition of atomic center-of-mass (CM) states perturbatively in terms of the dynamic of the electric field coupled with the atomic internal structure through its dipole moment. In section 1.1 the complete evolution of a superposition of wavepackets interacting with the environment is derived. The influence functional is introduced, and from it the interferometric phase and decoherence are obtained. In second order of perturbation theory the phase is shown to be the sum of terms depending on each wavepacket individually (local) and on both of the wave packets (non-local). In section 1.2, these results are applied for the propagation of an atom in the dipole approximation. Writing the phase in terms of linear response functions allows for the separation in contributions from dipole and field fluctuations. The results of this chapter will be the starting point for the derivation of the quantum vacuum Sagnac effect (chapter 2).

## 1.1 Open-system theory for atom interferometers

Atom interferometers are implemented through the use of nanogratings or light pulses to create superpositions of atomic wavepackets (see [63] for a recent review). Each wavepacket is confined by a potential to propagate in a given region of space, creating atomic waveguides [64, 65]. The wave packets are then recombined by another light pulse, and the phase difference acquired by the temporal evolution on each waveguide is measured. During the whole process, the control is over the wave function of the CM, and any interaction with the environment cannot be controlled experimentally during atomic propagation. This motivates the development of an open-system description of atom interferometers.

For a single atom whose CM state is prepared as a coherent superposition of two

wave packets, each propagating through an interferometer path, the state of the system atom+environment at $t = 0$ is

$$|\psi(0)\rangle = \frac{1}{\sqrt{2}}(|\psi^1_{CM}(0)\rangle + |\psi^2_{CM}(0)\rangle) \otimes |\psi_E(0)\rangle\,, \tag{1.1}$$

with $|\psi^k_{CM}(0)\rangle$ being the wavepacket for the path $k = 1, 2$. The initial state of the environment is $|\psi_E(0)\rangle$, the ground state of the uncoupled environment Hamiltonian $H_E$. The coupling with other degrees of freedom on the atom's surroundings is described by the interaction Hamiltonian $H_{int}(\mathbf{r}_A(t))$, with $\mathbf{r}_A(t)$ being the atomic position operator. The total Hamiltonian of the system is $H = H_{CM} + H_E + H_{int}$, with $H_{CM}$ being the Hamiltonian of the free propagation of the atomic CM. If the width of the wave packets is much smaller than the typical lengths associated to the interaction, the position operator in the Hamiltonian can be substituted by its instantaneous average for each wavepacket $\mathbf{r}_k(t) = \langle r_A(t)\rangle_k$.[1]

Given the negligible width approximation, $H_{int}(\mathbf{r}_k(t))$ only acts on environmental states. The total state of the system after an interaction time $T$ is [66]

$$|\psi(T)\rangle = \frac{1}{\sqrt{2}}\,|\psi^1_{CM}(T)\rangle \otimes \mathcal{T} e^{\frac{-i}{\hbar}\int_0^T dt \tilde{H}_{int}(\mathbf{r}_1(t))}\,|\psi_E(0)\rangle + \frac{1}{\sqrt{2}}\,|\psi^2_{CM}(T)\rangle \otimes \mathcal{T} e^{\frac{-i}{\hbar}\int_0^T dt \tilde{H}_{int}(\mathbf{r}_2(t))}\,|\psi_E(0)\rangle\,. \tag{1.2}$$

Here, $\mathcal{T}$ is the time-ordering operator and $\tilde{H}_{int}$ is the Hamiltonian in the interaction picture

$$\tilde{H}_{int}(\mathbf{r}_i(t)) = e^{\frac{i}{\hbar}H_E t} H_{int}(\mathbf{r}_i(t)) e^{-\frac{i}{\hbar}H_E t}. \tag{1.3}$$

The wavepacket $|\psi^k_{CM}(T)\rangle$ is obtained by the free evolution with $H_{CM}$.

Since the environmental degrees of freedom are not accessible experimentally, we can work with the reduced density matrix in order to derive the relative phase obtained from dynamics of each wavepacket interacting with the environment, by analyzing its off-diagonal elements. We thus take the partial trace of the density matrix

[1] The inclusion of finite width effects is discussed in Ref. [54].

$\rho(T) = |\psi(T)\rangle \langle\psi(T)|$ over the environment states, represented by $\mathrm{Tr_E}$. The reduced density matrix is

$$\rho_E(T) = \mathrm{Tr}_E \, |\psi(T)\rangle \langle\psi(T)| \, . \tag{1.4}$$

Using as basis the eigenstates of $H_E$, labeled as $|n_E\rangle$, we obtain the following expression by applying Eq.(1.2)

$$\begin{aligned} \rho_E(T) = \frac{1}{2} \sum_{n_E} \; & |\psi^1_{CM}(T)\rangle \langle\psi^1_{CM}(T)| \langle\psi^1_E(T)|n_E\rangle \langle n_E|\psi^1_E(T)\rangle \\ & + |\psi^1_{CM}(T)\rangle \langle\psi^2_{CM}(T)| \langle\psi^2_E(T)|n_E\rangle \langle n_E|\psi^1_E(T)\rangle \\ & + |\psi^2_{CM}(T)\rangle \langle\psi^1_{CM}(T)| \langle\psi^1_E(T)|n_E\rangle \langle n_E|\psi^2_E(T)\rangle \\ & + |\psi^2_{CM}(T)\rangle \langle\psi^2_{CM}(T)| \langle\psi^2_E(T)|n_E\rangle \langle n_E|\psi^2_E(T)\rangle \, , \end{aligned} \tag{1.5}$$

where $|\psi^k_E(T)\rangle = \mathcal{T} e^{\frac{-i}{\hbar}\int_0^T dt \tilde{H}_{int}(\mathbf{r}_k(t))} |\psi_E(0)\rangle$ represents the time evolution of environmental states along each atomic path. Using the closure relation of the basis, the reduced density matrix becomes

$$\begin{aligned} \rho_E(T) = \frac{1}{2}( & |\psi^1_{CM}(T)\rangle \langle\psi^1_{CM}(T)| + |\psi^1_{CM}(T)\rangle \langle\psi^2_{CM}(T)| \langle\psi^2_E(T)|\psi^1_E(T)\rangle \\ & + |\psi^2_{CM}(T)\rangle \langle\psi^1_{CM}(T)| \langle\psi^1_E(T)|\psi^2_E(T)\rangle + |\psi^2_{CM}(T)\rangle \langle\psi^2_{CM}(T)|). \end{aligned} \tag{1.6}$$

Therefore, one finds the interference term representing the coherences of the atomic CM (in position representation) to be

$$\rho_{12}(\mathbf{r}, \mathbf{r}', T) = \frac{1}{2} \psi^1_{CM}(\mathbf{r}, T) \psi^{2*}_{CM}(\mathbf{r}', T) \langle\psi^1_E(T)|\psi^2_E(T)\rangle \, , \tag{1.7}$$

Note that Eq. (1.7) apart from the internal product $\langle\psi^1_E(T)|\psi^2_E(T)\rangle$ is the interference term without interaction, and hence the off-diagonal elements of the reduced density matrix can be written as a product of a free-propagating term and an interaction term

$$\rho_{12}(\mathbf{r}, \mathbf{r}', T) = \rho^{(0)}_{12}(\mathbf{r}, \mathbf{r}', T) e^{i\Phi_{12}}, \tag{1.8}$$

with

$$\begin{aligned} \rho^{(0)}_{12}(\mathbf{r}, \mathbf{r}', T) &:= \frac{1}{2} \psi^1_{CM}(\mathbf{r}, T) \psi^{2*}_{CM}(\mathbf{r}', T) \\ e^{i\Phi_{12}} &:= \langle\psi^1_E(T)|\psi^2_E(T)\rangle \, . \end{aligned} \tag{1.9}$$

The term $e^{i\Phi_{12}}$ contains information on the interaction with the environment and measures this effect on the coherence. Due to the open system approach, the evolution is not unitary and therefore $\Phi_{12}$ is not a real number. However, both real and imaginary parts have interesting physical interpretations. The real part is the displacement in the interference pattern caused by the interaction, which is the focus of this chapter, while the imaginary part corresponds to the loss of visibility of interference fringes, indicating that information is lost by the entanglement between the degrees of freedom. The imaginary part of $\Phi_{12}$ leads to an exponential decay of the off diagonal elements of the reduced density matrix. This is known as decoherence, a consequence of the different interactions with the wavepackets that allow for "which path" information, and has been studied in the context of the Casimir effect [67], DCE [68] and QF [29, 69].

We obtain the overlap of the environment states using time-dependent perturbation theory in the interaction picture. Using a second-order Dyson expansion, one finds

$$\begin{aligned} e^{i\Phi_{12}} &= 1 + \frac{i}{\hbar}\int_0^T \langle H_{int}(\mathbf{r}_2(t))\rangle_0\, dt - \frac{i}{\hbar}\int_0^T \langle H_{int}(\mathbf{r}_1(t))\rangle_0\, dt \\ &+ \frac{1}{\hbar^2}\int_0^T\int_0^T \langle H_{int}(\mathbf{r}_2(t'))H_{int}(\mathbf{r}_1(t))\rangle_0\, dt'dt \\ &- \frac{1}{\hbar^2}\int_0^T\int_0^t \langle H_{int}(\mathbf{r}_2(t'))H_{int}(\mathbf{r}_2(t))\rangle_0\, dt'dt - \frac{1}{\hbar^2}\int_0^T\int_0^t \langle H_{int}(\mathbf{r}_1(t))H_{int}(\mathbf{r}_1(t'))\rangle_0\, dt'dt. \end{aligned} \tag{1.10}$$

The quantum averages $\langle ... \rangle_0$ are with respect to the initial unperturbed environment state. From Eq. (1.10), that are two different contributions to $e^{i\Phi_{12}}$ on the second order terms: integrals that depend on the Hamiltonian for each path separately (the last of Eq. (1.10)), connecting points of the same trajectory at different times (the local term or single path), and a term containing information of both paths simultaneously that cannot be separated into contributions from each path, called nonlocal (or double path). The crosstalk between paths arises as a consequence of environmental perturbation on a superposition rather than on an individual point-like moving atom.

## 1.2 Local and nonlocal dynamical Casimir phases

The previous section presented general results for the phase acquired by an atom as a footprint of the interaction with other degrees of freedom of the complete system. Here, those results are applied for an atom coupled with the quantum electric field through its dipole moment. The corresponding Hamiltonian is

$$H_{int} = -\mathbf{d}(t) \cdot \mathbf{E}(\mathbf{r}_k(t), t), \tag{1.11}$$

where $\mathbf{E}(\mathbf{r}_k(t), t)$ is the electric field operator evaluated on the atom CM position and $\mathbf{d}(t)$ is the atomic electric dipole moment operator. This Hamiltonian connects three set of degrees of freedom: the atomic CM, represented by $\mathbf{r}_k(t)$, the internal atomic structure given by the dipole operator $\mathbf{d}(t)$ and the electric field $\mathbf{E}(\mathbf{r}, t)$. The initial environment state is the tensor product of the internal atomic state $|\psi_A\rangle$ and the field state $|\psi_F\rangle$:

$$|\psi_E(0)\rangle = |\psi_A(0)\rangle \otimes |\psi_F(0)\rangle \tag{1.12}$$

Here, the initial states for the internal atomic degree of freedom and the field are the ground state and vacuum, respectively. This is the ground state of $H_E = H_A + H_F$, where $H_A$ is the Hamiltonian of the atomic internal structure and $H_F$ is the Hamiltonian of the free field.

An atom in its ground state does not have a permanent dipole moment. This implies that the first order terms in the Dyson series of Eq. (1.10) vanishes. In addition, considering small induced coherences [57, 58] it is possible to use the first order expansion $e^{i\Phi_{12}} \approx 1 + i\Phi_{12}$. Equation (1.10) then becomes

$$\begin{aligned}\Phi_{12} = &\frac{1}{i\hbar^2}\int_0^T\int_0^T \langle d_i(t')d_j(t)\rangle \langle E_i(\mathbf{r}_2(t'))E_j(\mathbf{r}_1(t))\rangle \\ &- \frac{1}{i\hbar^2}\int_0^T\int_0^t \langle d_i(t')d_j(t)\rangle \langle E_i(\mathbf{r}_1(t))E_j(\mathbf{r}_1(t'))\rangle - \frac{1}{i\hbar^2}\int_0^T\int_0^t \langle d_i(t')d_j(t)\rangle \langle E_i(\mathbf{r}_2(t'))E_j(\mathbf{r}_2(t))\rangle .\end{aligned} \tag{1.13}$$

If a classical object is placed near an atomic path, the Casimir interaction with the atom changes the dipole and field fluctuations, and therefore the correlation functions

in Eq. (1.13) carry information on the object due to scattering. This can be shown explicitly by writing the correlation functions in terms of the system's response functions (see appendix A). In order to do so, the second order correlation function is written as a sum of commutator and anticommutator of the operators:

$$\langle A(x)A(x')\rangle = \frac{1}{2}(\langle [A(x), A(x')]\rangle + \langle \{A(x), A(x')\}\rangle). \tag{1.14}$$

The average of the antincommutator (or symmetric correlation function) stand for the fluctuations of the observable $A$. It corresponds to the Hadamard Green's function:

$$G^H_{\mathbf{A}ij}(x, x') = \frac{1}{\hbar}\left\langle \{A_i(x), A_j(x')\}\right\rangle . \tag{1.15}$$

Furthermore, the susceptibilities of field and dipole are defined in terms of commutators (see Eqs. (A.15) and (A.13) from appendix A), namely:

$$\begin{aligned} \alpha^A_{mn}(t, t') &:= \frac{i}{\hbar}\theta(t - t')\left\langle [d_m(t), d_n(t')]\right\rangle \\ G^R_{mn}(\mathbf{r}_k(t), t; \mathbf{r}_l(t'), t') &:= \frac{i}{\hbar}\theta(t - t')\left\langle [E_m(\mathbf{r}_k(t), t), E_n(\mathbf{r}_l(t'), t')]\right\rangle , \end{aligned} \tag{1.16}$$

where $k$ and $l$ label the atom interferometer path, $k, l = 1, 2$. The polarizability depends on the atomic internal state. For all the discussions in this thesis, the polarizability is for the ground-state. The field retarded Green's function is the field propagator. The commutators in terms of response functions are

$$\begin{aligned} [d_m(t), d_n(t')] &= \frac{\hbar}{i}(\alpha^A_{mn}(t, t') - \alpha^A_{nm}(t', t)) \\ [E_m(\mathbf{r}_k(t), t), E_n(\mathbf{r}_l(t), t)] &= \frac{\hbar}{i}(G^R_{mn}(\mathbf{r}_k(t), t; \mathbf{r}_l(t'), t') - G^R_{nm}(\mathbf{r}_l(t'), t'; \mathbf{r}_k(t), t)). \end{aligned} \tag{1.17}$$

In the presence of a neutral object, the electric field is the sum of the free and scattered fields. The retarded Green's function is the sum of a direct propagation of a dipole field and a scattered assisted propagation:

$$G^R_{mn}(\mathbf{r}_k(t), t; \mathbf{r}_l(t'), t') = G^{R,(0)}_{mn}(\mathbf{r}_k(t), t; \mathbf{r}_l(t'), t') + G^{R,S}_{mn}(\mathbf{r}_k(t), t; \mathbf{r}_l(t'), t'), \tag{1.18}$$

on which $G^{R,(0)}_{mn}(\mathbf{r}_k(t), t; \mathbf{r}_l(t'), t')$ is the free-space Green's function, propagating field produced by a dipole at position $\mathbf{r}_l(t')$ and time $t'$ to the position $\mathbf{r}_k(t)$ at instant $t$, and

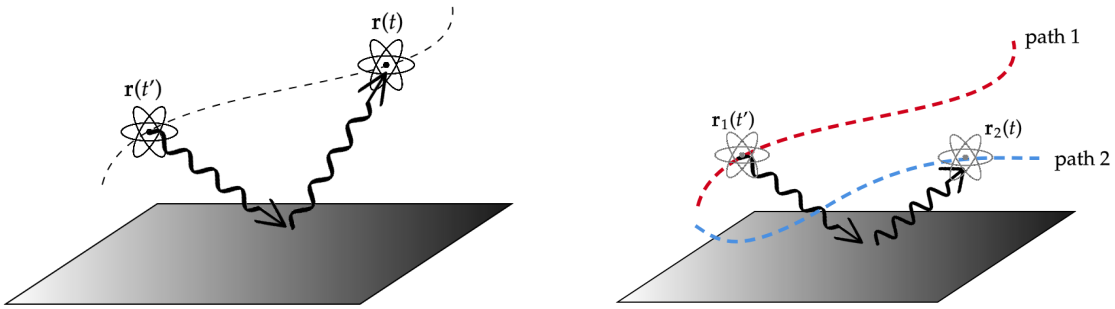


(a) (b)

Figure 1.1: (a) Schematization of a field produced by the atom at position $\mathbf{r}(t')$ and instant $t'$ to propagating to a surface. The scattered field reaches the atom at another position $\mathbf{r}(t)$ at a later instant $t$. This surface mediated propagation is described by the scattered Green's function $G^{R,S}_{mn}(\mathbf{r}_k(t), t; \mathbf{r}_l(t'), t')$. (b)Representation of the physical mechanism behind the nonlocal term. Scattering allows for a joint contribution from the two paths.

$G^{R,S}_{ij}(\mathbf{r}_k(t), t; \mathbf{r}_l(t'), t')$ is the scattered Green's function, representing the field propagation mediated by object (see figure 1.1a). The field produced by the dipole at $(\mathbf{r}_l(t'), t')$ propagates to the object, polarizing it. The induced dipole propagates to spacetime point $(\mathbf{r}_k(t), t)$. The scattered Green's function is the term producing the Casimir phase, as the free space contribution exists even without anything in the neighborhood of the atom interferometer, and therefore the contribution from $G^{R,(0)}_{mn}(\mathbf{r}_k(t), t; \mathbf{r}_l(t'), t')$ will not be included in calculations henceforth. The same reasoning applies to the Hadamard Green's function for the field. This has been used to calculate local and nonlocal phases for an atom interferometer near a perfectly conducting plane [54]. In that sense, the nonlocal contributions occur when a virtual photon produced by the atom on a path is scattered and then absorbed by the atom on another path (see figure 1.1b)

To obtain the phase associated with the interaction, it is necessary to take the real part of Eq. (1.13). Since the average of the anticommutator of two given hermitian operators is a real number, and the average of the commutator of the same operators is

purely imaginary, the measurable phase difference is

$$\Delta\phi_{12} := \mathrm{Re}\Phi_{12} = \varphi_{22} - \varphi_{11} + \varphi_{21} - \varphi_{12}$$
$$\varphi_{kl} := \frac{1}{4}\int\int_0^T dtdt'[g^H_{\mathbf{d}}(t,t')\mathcal{G}^{R,S}(\mathbf{r}_k(t),t;\mathbf{r}_l(t'),t') + \alpha^A(t,t')\mathcal{G}^{H,S}(\mathbf{r}_k(t),t;\mathbf{r}_l(t'),t')]. \tag{1.19}$$

The isotropy of the atom was considered to write the polarizability and the dipole Hadamard Green's function as multiples of the identity matrix: $\alpha^A_{mn}(t,t') = \alpha^A(t,t')\delta_{mn}$ and $G^H_{\mathbf{d}mn}(t,t') = g^H_{\mathbf{d}}(t,t')\delta_{mn}$. The result of the summation over indexes $i$ and $j$ is the trace of the retarded (and Hadamard) Green's function $\mathcal{G}^{R(H),S}(\mathbf{r}_k(t),t;\mathbf{r}_l(t'),t')$. For $k = l$, one has single path phases $\Delta\phi_{SP} = \varphi_{22} - \varphi_{11}$, while $k \neq l$ corresponds to double path phases $\Delta\phi_{DP} = \varphi_{21} - \varphi_{12}$. The first term of the integrated contains the dipole Hadamard Green's function and the field response function, and thus corresponds to the dipole fluctuations contribution. The second term contains the response of the atom to the field by the polarizability and the Hadamard Green's function for the field, representing the field fluctuations [70], which becomes relevant when the field retardation is non-negligible.

# Chapter 2

# Quantum vacuum Sagnac effect

The Sagnac effect occurs when a frame attached to an interferometer rotates relative to an inertial frame. As a consequence, an interferometric phase proportional to the angular velocity of rotation and the area enclosed by the interferometer arises. It was first proposed and measured by Georges Sagnac in 1913 [55], and is the basis for the operation of ring laser gyroscopes, which to this day are used in high-precision inertial navigation. However, the Sagnac effect occurs with different wave phenomena, such as sound [71] and matter waves [72–77]. For the latter, the phase acquired by the rotation of the interferometer depends on the mass of the quantum objects and allows for a higher resolution compared to the optical Sagnac effect [78–81], which relies on relativistic effects. Recent experiments with cold atom interferometry detected angular velocities with precision on the order of $10^{-11}$ rad/s [82].

Considering the high precision of atom interferometers and the fast rotation of nanoparticles achieved in recent experiments [44], the following question arises: could there be a detectable atomic phase related to the rotation of a neutral particle in between the interferometer's arms? Such an effect would be analogous to the Sagnac effect, but instead of a rotation of the whole apparatus, the phase is originated by the interaction with the spinning objects in its neighborhood, leading to the persistence of a noninertial effect into the inertial frame. In that case, the interaction is mediated by quantum vacuum fluctuations, and the associated phase shall henceforth be called the quantum vacuum

Sagnac phase (QVSP). In this regard, the QVSP is also analogous to the DCE and the QF, as the relative propagation of interfering wavepackets with respect to the sense of the particle's rotations is pivotal to the effect. However, contrary to those effects, the QVSP occurs without the emission of real photons. In addition, for experimental ultrahigh rotation frequencies [2, 44, 46], the QVSP is at the limit of sensitivity of state-of-the-art atom interferometers [81, 83], while the photon emission rate by the dynamical Casimir effect is typically too small to allow any measurement with current technologies. [84–86].

This chapter presents a derivation of the QVSP and a discussion of its properties. In section 2.1, the interferometric phase for an atom propagating near a rotating nanoparticle is calculated using the results from the previous chapter and shown to be a geometric Berry phase [87] proportional to the angular velocity of rotation. The result allows for an analogy between the QVSP and the Aharonov-Bohm effect (ABE) [88]. Section (2.2) presents estimations of the phase for realistic experimental parameters, with results for the case of finite-size wavepackets. If the atomic transition frequency is close to the plasmon resonance, it is shown that the magnitude of the QVSP is within the limit of precision of modern atom interferometers. In section 2.3 the force on the atom is calculated, and the result is shown to be analogous to the Coriolis force. Given the plasmon resonance regime, the force on the atom is of the same order as other single-atom measurements.

## 2.1 Quantum vacuum Sagnac phase

To model the system, we consider a ground-state two-level atom (with transition frequency $\omega_0$) whose CM propagation is described by the quantum superposition of two very narrow wavepackets, each corresponding to an interferometer arm. In the vicinity of the interferometer, there is a nanoparticle spinning with constant angular frequency $\mathbf{\Omega}$. In addition, the rotation velocity is parallel to the nanoparticle's symmetry axis[1], which is the case of the experiments in Refs. [2, 44, 46]. We consider a spherical particle for all the

[1]The case when the rotation is perpendicular to the symmetry axis is discussed in Chapter 3.

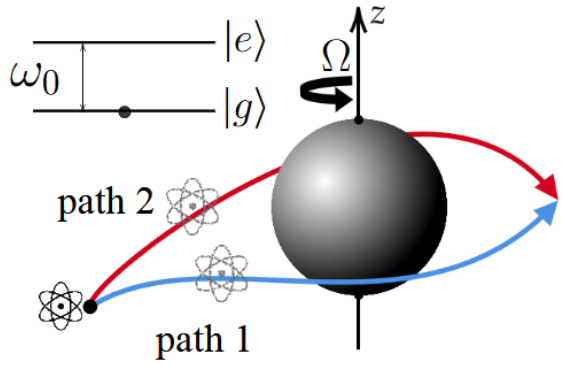


Figure 2.1: Scheme of the quantum vacuum Sagnac interferometer. The CM of a ground-state atom propagates as a quantum superposition of two wave packets around a spinning neutral nanoparticle (angular frequency $\mathbf{\Omega}$). Figure from Ref. [1]

.

applications in this chapter. The modification in the atom-nanoparticle interaction due to the relative rotation arises from the dispersive behavior of its dielectric function.

It is important to note that this system does not present real photon emission, as the atom is in its ground state and a uniform rotating dielectric sphere does not emit DCE [89] or QF photons [50,51]. Although the absorption of the sphere's material leads to quantum radiation emission, it is not a requirement for QVSP, which can still be nonzero with only virtual photons.

### 2.1.1 Expression of the quantum vacuum Sagnac phase in terms of Green's functions

We use the formalism and results presented in Chapter 1 for atomic waves presenting a dipolar interaction with the electromagnetic field. From Eq. (1.19):

$$\Delta\phi_{12} = \varphi_{11} - \varphi_{22} + \varphi_{12} - \varphi_{21} \tag{2.1}$$

$$\varphi_{kl} = \frac{1}{4}\int\int_{-T/2}^{T/2} dtdt' [g^H_{\mathbf{d}}(t,t')\mathcal{G}^{R,S}(\mathbf{r}_k(t),t;\mathbf{r}_l(t'),t') + \alpha^A(t,t')\mathcal{G}^{H,S}(\mathbf{r}_k(t),t;\mathbf{r}_l(t'),t')]. \tag{2.2}$$

The first approximation is to consider that the typical atom-nanoparticle distances are small compared to the wavelengths of the atomic transition. This allows us to work

in the non-retarded (or van der Waals (VdW)) regime, where the propagation time of the electric field is negligible. Within this approximation, the contribution from field fluctuations becomes negligible near the nanoparticle, and the first term of equation (2.2) is the only relevant term for the phase. The quantum field fluctuations are relevant for wavelengths of the order of the atom-particle distance, which typically correspond to frequencies at which both the atom and the particle do not exhibit appreciable dispersive behavior. As discussed later in this Section, dispersion is a key effect to the existence of the QVSP, and thus the inclusion of retardation effects does not change the QVSP considerably.

For a 2-level atom, the Hadamard Green's function is given by [54]

$$g^H_{\mathbf{d}}(t,t') = \alpha_0^A \cos(\omega_0(t-t')), \tag{2.3}$$

with $\alpha_0^A$ being the static atomic polarizability and $\omega_0$ being the transition frequency. The other correlation function necessary to compute the QVSP is the scattered retarded Green's function $G^{R,S}_{\mathbf{E}ij}(\mathbf{r},t;\mathbf{r}',t')$. The scattering occurs between the instants $t'$ and $t$. Assuming that the nanoparticle's dimensions are much smaller than the wavelengths of atomic transitions, the other multipolar contributions to the scattering other than the electric dipole become negligible (dipole approximation), and thus the scattered retarded Green's function can be written in terms of the particle's polarizability. Since rotation changes its electric response, the modified polarizability tensor is indicated as $\boldsymbol{\alpha}^{\boldsymbol{\Omega}}$. Considering the nanoparticle at the origin of the coordinate system, the corresponding Green's function in the frequency domain ($\mathbf{G}^{R,S}_{\mathbf{E}}(\mathbf{r},\mathbf{r}',\tau) = \frac{1}{2\pi}\int d\omega e^{-i\omega\tau}\mathbf{G}^{R,S}_{\mathbf{E}}(\mathbf{r},\mathbf{r}',\omega)$) is

$$\mathbf{G}^{R,S}_{\mathbf{E}}(\mathbf{r},\mathbf{r}',\omega) = \mathbf{G}^{R,0}(\mathbf{r},0,\omega)\cdot\boldsymbol{\alpha}^{\boldsymbol{\Omega}}(\omega)\cdot\mathbf{G}^{R,0}(0,\mathbf{r}',\omega). \tag{2.4}$$

Equation (2.4) represents a double propagation for the electric field of a dipole. The first comes from the atom at a position $\mathbf{r}'$ to the nanoparticle, which becomes polarized and produces a field that propagates to the atom at position $\mathbf{r}$ (see Figure (2.2)).

Here, $\mathbf{G}^{R,0}(\mathbf{r},\mathbf{r}',\omega)$ is the free-space retarded Green's function [90, 91] (see Eq. (A.18) in Appendix A). In the vdW regime, its expression is

$$G^{R,0}_{mn}(\mathbf{r},\mathbf{r}',\omega) \approx (3R_iR_j/R^2 - \delta_{mn})/(4\pi\epsilon_0 R^3), \tag{2.5}$$

with $\mathbf{R} = \mathbf{r} - \mathbf{r}'$. Eq. (2.5) can be obtained by taking the limit $kR \ll 1$ in Eq. (A.18). Since the scattered field $\mathbf{E}^{scat}(\mathbf{r},\omega)$ is an induced dipole field, we have

$$\mathbf{E}^{scat}(\mathbf{r},\omega) = \mathbf{G}^{R,0}(\mathbf{r},\mathbf{0},\omega)\cdot\mathbf{d}^{ind,\Omega}(\omega), \tag{2.6}$$

with $\mathbf{d}^{ind,\Omega}(\omega)$ being the induced dipole of the rotating nanoparticle. Combining Eq. (2.6) with the constitutive relations for the induced dipole and dipole field, namely (see Appendix A)

$$\begin{aligned}\mathbf{d}^{ind}(\omega) &= \boldsymbol{\alpha}^{\boldsymbol{\Omega}}(\omega)\cdot\mathbf{E}^{ind}(\mathbf{0},\omega)\\ \mathbf{E}^{ind}(\mathbf{0},\omega) &= \mathbf{G}^{R,0}(\mathbf{0},\mathbf{r}',\omega)\cdot\mathbf{d}(\omega),\end{aligned} \tag{2.7}$$

we obtain the scattered Green's function from Eq. (2.4).

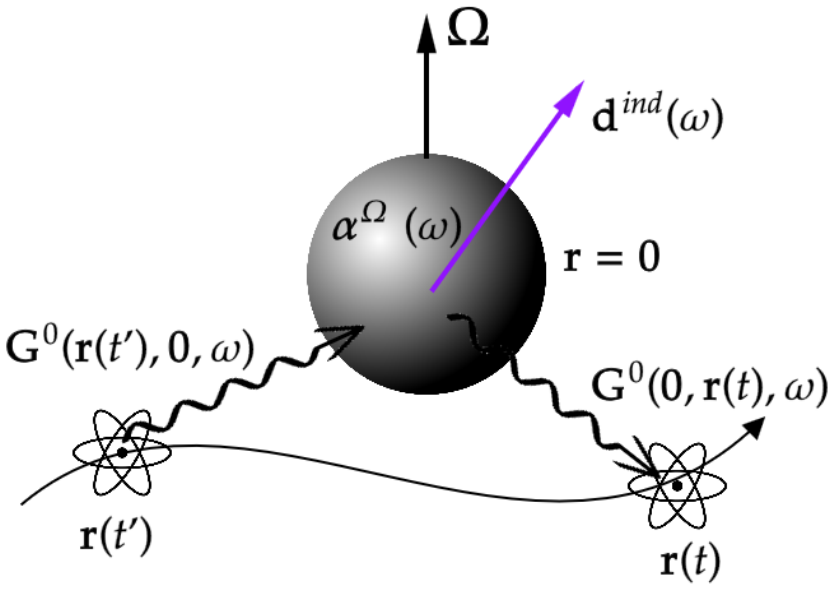


Figure 2.2: Schematization of the scattered Green's function: the atom produces a field at the position $\mathbf{r}(t')$ that propagates to the position of the nanoparticle polarizing it. The induced dipole (purple vector) produces a field that reaches the atom on another position $\mathbf{r}(t)$.

The remaining component necessary to compute the QVSP is the polarizability for a rotating object. This is done following the semiclassical approach in Ref. [50] (see Appendix B for a detailed discussion). For an isotropic nanoparticle at rest, the polarizability tensor is $\boldsymbol{\alpha}^0(\omega) = \tilde{\alpha}(\omega)\mathbb{1}$. The rotation breaks isotropy, and off-diagonal terms arise in the polarizability tensor as a consequence. For a non-relativistic angular velocity vector $\boldsymbol{\Omega}$, the polarizability for a rotating spherical particle is given by [50]

$$\delta\alpha^{\boldsymbol{\Omega}}_{lm}(\omega) = \alpha^{\boldsymbol{\Omega}}_{lm}(\omega) - \alpha^{0}_{lm}(\omega) \approx i\tilde{\alpha}'(\omega)\sum_n \epsilon_{lmn}\Omega_n, \tag{2.8}$$

where $\tilde{\alpha}'(\omega)$ is the frequency derivative of the degenerate polarizability eigenvalue and $\epsilon_{lmn}$ is the Levi-Civita symbol. The approximation considered the angular frequency much smaller than the typical frequencies at which the polarizability varies appreciably. The effect of rotation on the electric response of the particle occurs only due to the frequency dispersion of the material. This result is central to the existence of the QVSP.

### 2.1.2 Analytic expression for the Quantum Vacuum Sagnac Phase

The computation of the integral in Eq. (2.2) involves different time scales. Given the Van der Waals approximation, the relevant times are listed from the largest to the smallest scale:

- the interaction time $T$ of the atom on the interferometer ($\sim 10^{-3}\,\mathrm{s}$ [64]),
- the period of the nanoparticle's GHz rotation, $2\pi/\Omega$ ($\sim 10^{-10}\,\mathrm{s}$ [44]),
- the period of atomic oscillation, $2\pi/\omega_0$ ($\sim 10^{-15}\,\mathrm{s}$ for the $3s_{1/2} - 3p_{3/2}$ transition of sodium atoms)
- the time delay due to dispersion of the nanoparticle's material, $2\pi/\omega_p$ ($\sim 10^{-15}\,\mathrm{s}$ for potassium particles [92]),
- the propagation time of the field from the atom to the sphere, $r/c$ ($\sim 10^{-17}\,\mathrm{s}$).

Where $\omega_p$ is the plasma frequency of the material. This disparity in time scales allows for some approximations to be taken. First, noticing that the polarizability in the the scattered Green's function determines that the relevant contribution comes from time intervals of the order of the particle response time, it is possible to neglect the acceleration of the atomic CM during those intervals, and thus $\mathbf{r}_l(t') \approx \mathbf{r}_l(t) - (t-t')\mathbf{v}_l(t)$, with $\mathbf{v}_l(t)$ representing the CM velocity on the path $l$.

Furthermore, the displacement of atomic waves during $t - t'$ is much smaller than the wavelength contributing to the electric field Green's function ($2\pi c/\omega_0$), allowing for a first-order Taylor expansion of the scattered Green's function around $\mathbf{r}_l(t)$:

$$\mathcal{G}_{\mathbf{E}}^{R,S}(\mathbf{r}_k(t),t;\mathbf{r}_l(t'),t') \approx \mathcal{G}_{\mathbf{E}}^{R,S}(\mathbf{r}_k(t),t;\mathbf{r}_l(t),t') - (t-t')\mathbf{v}_l(t)\cdot\nabla_{\mathbf{r}'}\mathcal{G}_{\mathbf{E}}^{R,S}(\mathbf{r}_k(t),t;\mathbf{r}',t')\Big|_{\mathbf{r}'=\mathbf{r}_l(t)}. \tag{2.9}$$

The first term produces a quasistatic phase, as it depends only on the instantaneous position of the atom in each interferometer path. On the other hand, the second term is associated with a phase that relies on the movement of the atomic CM. The QVSP $\phi_{kl}^{\Omega}$ is thus a sum of the quasistatic and the motional phases. However, the quasistatic term does not contribute to the phase associated to the nanoparticle rotation, as the contraction between the free-space Green's function (symmetric) and the rotating particle polarizability tensor (antisymmetric) vanishes. Therefore, the QVSP is solely induced by the atomic movement during the time of propagation of virtual photons being traded between the atom and the nanoparticle.

Considering that the time $T$ of flight of the atom in the vicinity of the particle is much longer than the period of atomic oscillation ($\omega_0 T \gg 1$) and using the approximations above together with the dipole Hadamard Green's function (Eq. (2.3)), Eq. (2.2) simplifies to

$$\phi_{kl}^{\Omega} = -\frac{\alpha_0^A\omega_0}{4}\int_{T/2}^{T/2} dt\mathbf{v}_k(t)\cdot\partial_\omega\nabla_{\mathbf{r}'}\mathrm{Im}[\delta\mathcal{G}_{\mathbf{E}}^{\mathrm{R,S}}(\mathbf{r},\mathbf{r}',\omega)]. \tag{2.10}$$

The gradient is taken at $\mathbf{r} = \mathbf{r}_k(t), \mathbf{r}' = \mathbf{r}_l(t)$ and the frequency derivative at $\omega = \omega_0$.

$\delta\mathcal{G}^{R,S}_{\mathbf{E}}(\mathbf{r},\mathbf{r}',\omega)]$ indicates the contributions to the scattered Green's function that contains the angular frequency $\mathbf{\Omega}$. The frequency derivative is related to the time delay associated with the electric response of the nanoparticle along the CM movement.

Casting Eqs. (2.5) and (2.8) in Eq. (2.10) results in the general expression for the local contribution to QVSP as a geometric integral:

$$\phi_k^{\Omega} = \frac{9}{4}\frac{\alpha_0\omega_0 \mathrm{Re}[\tilde{\alpha}''(\omega_0)]}{(4\pi\epsilon_0)^2}\int_{\mathcal{P}_k} d\mathbf{r}\cdot\frac{\mathbf{\Omega}\times\mathbf{r}}{r^8}. \tag{2.11}$$

The integral is calculated along the interferometer path $\mathcal{P}_k$, with initial and final points $\mathbf{r}_k(-T/2)$ and $\mathbf{r}_k(T/2)$. Eq. (2.11) shows that the quantum vacuum Sagnac effect is analogous to the standard Sagnac effect [93–95], since both phases are given by line integrals proportional to the angular velocity $\Omega$[2]. Eq. (2.11) can be generalized for an atom with many energy levels [96]:

$$\phi_k^{\Omega} = \sum_e \frac{3|\mathbf{d}_{eg}|^2 \mathrm{Re}[\tilde{\alpha}''(\omega_{\mathrm{eg}})]}{\hbar(4\pi\epsilon_0)^2}\int_{\mathcal{P}_k} d\mathbf{r}\cdot\frac{\mathbf{\Omega}\times\mathbf{r}}{r^8}, \tag{2.12}$$

where $\sum_e$ is the sum over excited states, $\mathbf{d}_{eg}$ is the dipole moment of the transition from the ground state to the state $|e\rangle$, and $\omega_{eg}$ is the frequency of the transition.

Like the Sagnac effect [94,95,97], the QVSP has similarities with the Aharonov-Bohm effect [98], since Eq.(2.11) is given by the circulation of a geometric field analogous to the vector potential. Furthermore, in the Aharonov-Bohm effect, a magnetic flux confined to a solenoid produces a phase proportional to its magnitude on particles that propagate in a domain free of magnetic fields. Here, analogously, a rotation confined to the space occupied by the nanoparticle imprints a phase on the surrounding matter waves outside the rotation region.

Moreover, the local QVSP is a geometric phase, since it does not depend on the velocity of the atom, and changes sign by reversing the direction of propagation. The

[2] with the distinction that $\Omega$ is the angular velocity of the whole interferometer with respect to an inertial frame in the context of the Sagnac effect and $\Omega$ is the rotation frequency of a nanoparticle near the interferometer in the QVSP case

phase produced by the Sagnac effect property is also geometric [97]. This does not hold for the nonlocal term of the QVSP, since it depends on the instantaneous positions of both paths:

$$\phi_{kl}^{\Omega} = -\frac{\alpha_0^A \omega_0 \mathrm{Re}[\tilde{\alpha}''(\omega_0)]}{4(4\pi\epsilon_0)^2} \int_{-T/2}^{T/2} dt \frac{\boldsymbol{\xi}_{kl}(t) \cdot \boldsymbol{\Omega}}{r_k^3(t) r_l^4(t)}, \tag{2.13}$$

with $\boldsymbol{\xi}_{kl}(t)$ defined as

$$\boldsymbol{\xi}_{kl}(t) = [1 - 2(\hat{\mathbf{r}}_k \cdot \hat{\mathbf{r}}_l)]\,(\hat{\mathbf{r}}_k \cdot \mathbf{v}_l)\hat{\mathbf{r}}_k \times \hat{\mathbf{r}}_l + (\hat{\mathbf{r}}_k \cdot \hat{\mathbf{r}}_l)\hat{\mathbf{r}}_k \times \mathbf{v}_l. \tag{2.14}$$

To shed light on the geometric nature of the QVSP, it is possible to show that Eq.(2.11) is a Berry phase [87, 99] of the system 2-level atom + electric field. For a Hamiltonian parametrized by a vector $\mathbf{r}(t)$, an adiabatic evolution represented by a curve in the parameter space imprints a geometric phase on the eigenstate $|n(\mathbf{r}(t))\rangle$, called Berry (or Berry-Pancharatnam) phase. The Berry phase $\gamma_n$ for the corresponding eigenstate is obtained by the expression [99]

$$\gamma_n = \int_{\mathcal{C}} i \,\langle n(\mathbf{r}) | \nabla_{\mathbf{r}}\, n(\mathbf{r})\rangle \, d\mathbf{r}, \tag{2.15}$$

where $\mathcal{C}$ is a curve describing the evolution in the parameter space. As a geometric phase, the Berry phase does not depend on the rate at which the path is covered. The integrand is referred to as Berry connection or Berry potential. This kind of phase has been studied in the context of condensed matter physics [100], classical optics [101–103], molecular physics [104, 105], quantum field theory [106], and quantum gravity [107]. In our case, the continuous parameter of the Hamiltonian is the position vector, and the curve is the atomic path of the CM. An explicit demonstration showing that the QVSP is indeed a Berry phase is presented in appendix C.

## 2.2 QVSP in different configurations

### 2.2.1 Quantum Vacuum Sagnac Phase for specific geometric configurations

The dependence of the QVSP on the interferometer design can be illustrated by evaluating the integral in Eq. (2.11) for different atomic paths. For that purpose, two specific geometries are considered: semicircular concentric trajectories and two parallel lines. In both cases, the nanoparticle is in the center of the coordinate system and the angular frequency is $\mathbf{\Omega} = \Omega\hat{\mathbf{z}}$, with the $z$ axis perpendicular to the plane containing the trajectories (see Figure 2.3).

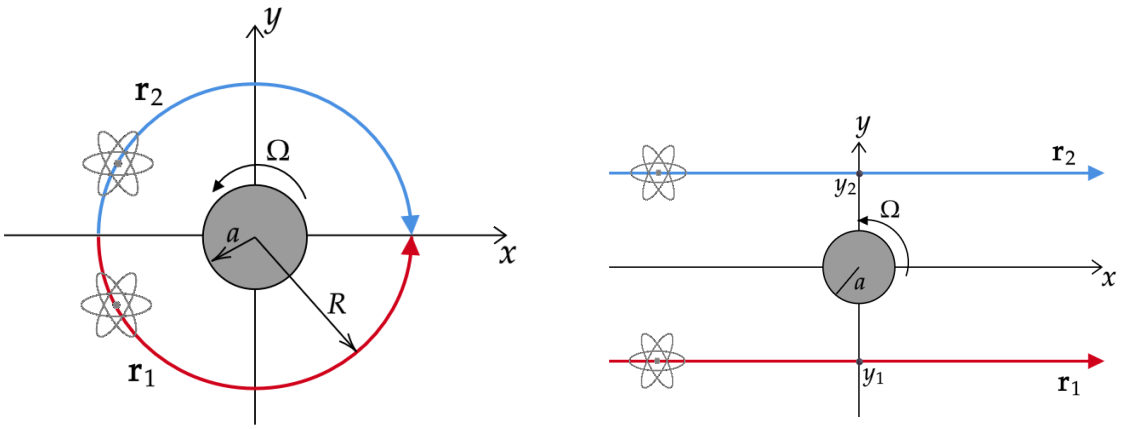


(a) (b)

Figure 2.3: Representation of the circular (a) and rectilinear (b) interferometers.

Although circular atom interferometers have been used in experiments involving the Sagnac effect [80], they operate based on confining potentials [64] that could be altered by the presence of the sphere. Therefore, this case is a textbook example for the QVSP. It is convenient to introduce the characteristic length $\ell_\Omega$, defined by

$$\ell_\Omega := \left| \frac{\alpha_0 \omega_0 \mathrm{Re}[\tilde{\alpha}''(\omega_0)]}{(4\pi\epsilon_0)^2} \right|^{1/6}, \tag{2.16}$$

by means of which the QVSP will be expressed. The local phase for the path with the

same sense of rotation as the nanoparticle is

$$\phi^{\Omega}_{circ} = \frac{9\pi}{2}\left(\frac{\ell_\Omega}{R}\right)^6. \tag{2.17}$$

Due to the geometric nature of the QVSP, the phase of the counterrotating path is $-\phi_{circ}$. For this geometry, the nonlocal term is zero.

On the other hand, rectilinear interferometers represent a more realistic approach towards experimental implementation, since colimated beams of atoms have been employed to detect dispersive effects [57, 59, 108]. For an atom moving along the $x$, the local phase for each path is

$$\phi^{\Omega}_{rec,k} = \frac{45\pi}{64}\left(\frac{\ell_\Omega}{r_{\perp k}}\right)^6 \frac{y_k}{r_{\perp k}}, \qquad r_{\perp k} = \sqrt{y_k^2 + z_k^2}. \tag{2.18}$$

the line segment $L$ traveled by the atom must obey the condition $|y_k|, |z_k| \ll L/2 \ll \lambda_0$ for consistency with the VdW approximation. A remarkable difference from the former case is that this geometry has a nonzero nonlocal phase. The double path phase has an opposite sign relative to the local term when considering the particle at the midpoint of the distance between trajectories ($y_2 = -y_1 = y_0$ and $z_1 = z_2 = 0$):

$$\phi^{\Omega}_{kl} = -\frac{27\pi(-1)^{k+1}}{128}\left(\frac{\ell_\Omega}{y_0}\right)^6, \quad k, l = 1, 2 \ (k \neq l), \tag{2.19}$$

and hence reduces the total QVSP difference to

$$\Delta\phi^{\Omega}_{rec} = \frac{63\pi}{64}\left(\frac{\ell_\Omega}{y_0}\right)^6 \mathrm{sgn}(y_0). \tag{2.20}$$

For this geometry, the nonlocal corresponds to approximately 30% of the total phase.

### 2.2.2 Plasmon resonance effects

Since the QVSP contains the second derivative of the sphere's polarizability evaluated on the atomic transition frequency (see Eq.(2.11)), the effect can be enhanced if the sphere is constituted by a material on which the polarizability is near or on a peak at the transition frequency $\omega_0$. This match is achieved if $\omega_0$ is the plasmon resonance

frequency [109] of the material, which occurs when a given frequency maximizes the sphere polarizability, given by

$$\tilde{\alpha}(\omega) = 4\pi\epsilon_0 a^3 \frac{\epsilon(\omega) - 1}{\epsilon(\omega) + 2}, \tag{2.21}$$

where $a$ is the sphere radius. The maximization occurs by minimizing the denominator. If the sphere is metallic, the most suitable model to describe the dielectric function is the Drude model, for which $\epsilon(\omega)$ is given by

$$\epsilon(\omega) = 1 - \frac{\omega_p^2}{\omega(\omega + i\gamma)}, \tag{2.22}$$

with $\omega_p$ being the plasma frequency and $\gamma$ the reciprocal electronic relaxation time. Within the dipole approximation, the plasma resonance frequency for a sphere is $\omega_{\text{res}} = \omega_p/\sqrt{3}$. However, for $\text{Re}[\tilde{\alpha}''(\omega)]$ the plasmon resonance peak is slightly shifted from $\omega_{\text{res}}$ due to the dissipation, and therefore $\omega_0$ must be close to this frequency without matching it. Considering Na atoms, for which the static polarizability is $\alpha_0^A/(4\pi\epsilon_0) = 2.4\times10^{-29}\,\text{m}^3$ and the dominant transition $3s_{1/2}-3p_{3/2}$ frequency is $\omega_0 = 3.198\times10^{15}\,\text{rad/s}$ [110], the plasma frequency that maximizes $\tilde{\alpha}''(\omega)$ is $\omega_p = 5.549\times10^{15}\text{rad/s}$. This value differs less than 1% from the plasma frequency of potassium [92], and thus the relaxation frequency $\gamma = 2.795\times10^{13}\,\text{rad/s}$ of potassium should be taken into account in the numerical calculations. Figure 2.4 presents the local QVSP for an atom in rectilinear trajectories (Eq.(2.20)) near a potassium sphere as a function of the frequency transition. The peaks are the plasmon resonances. For $y_0 = 10\,\text{nm}$ and $a = 5\,\text{nm}$ the local phase difference is $-0.3\,\text{mrad}$.

### 2.2.3 Quantum Vacuum Sagnac Phase for a wide atomic wavepacket

The results presented so far rely on the hypothesis that the width of the wave packets is very small compared to the distance between the atom and the nanoparticle, and thus the wave effects on the CM propagation become negligible. In order to explore the QVSP

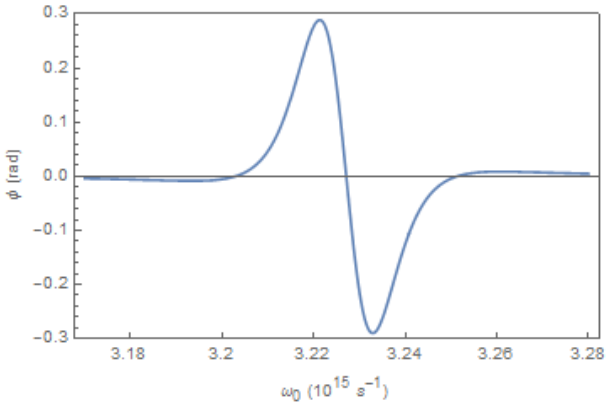


Figure 2.4: Local QVSP difference for two rectilinear trajectories with distance $y_0 = 10\,\text{nm}$ to a potassium sphere of radius $a = 5\,\text{nm}$ as a function of the atomic transition frequency $\omega_0$

in more realistic situations from an experimental point of view, the discussion henceforth shall be towards the estimation of the phase with finite-width atomic wave packets.

The inclusion of the finite width is done considering a Mach-Zender atomic interferometer, arranged in a way that only the local phase contributes to the QVSP by letting one path close to a rotating sphere of radius $a$ and the other path far away, eliminating non-local terms and local contributions from the second path. A similar configuration was used for the detection of vdW interactions through quasistatic phases [57, 59, 108]. The effect of the finite size of the CM wavepackets is obtained by averaging the atomic phase over its transverse width, as shown in Refs. [57, 108] in the context of quasistatic vdW phases. The total phase acquired by the atom is the sum of QVSP $\phi^{\Omega}$ and the aforementioned quasistatic phase $\phi^{\text{vdW}}$, obtained by integrating the instantaneous vdW potential along the CM trajectory. For an atom whose CM position is given by $\mathbf{r}(t) = x\hat{\mathbf{x}} + vt\hat{\mathbf{y}} + z\hat{\mathbf{z}}$, with $-L/2 \leq vt \leq L/2$, Equation ((2.2)) gives the known result [57]

$$\phi^{\text{vdW}}(y, z, v) = \frac{9\pi}{4}\alpha_0^A \omega_0 \tilde{\alpha}_R(\omega_0)/[(4\pi\epsilon_0)^2 v r_\perp^5], \tag{2.23}$$

with $r_\perp = \sqrt{y^2 + z^2}$. In contrast with the QVSP, the vdW phase remains unaffected by the sphere's rotation and is dynamical, since it is velocity-dependent.

To average the phase, one considers gaussian wavepackets propagating along the $x$-axis

with velocity $v$ at the edge of the nanosphere of radius $a$

$$\begin{aligned}\psi(x,y,z,t) &= \psi_\perp(y,z)\psi_\parallel(x,t)\\ \psi_\parallel(x,t) &= \frac{1}{\sqrt{\pi}w_\parallel}\exp\left(-\frac{(x-vt)^2}{2w_\parallel}\right)e^{\frac{i}{\hbar}mvx}\\ \psi_\perp(y,z) &= \frac{1}{\pi w^2}\exp\left(-\frac{[(y-a)^2+z^2]}{2w}\right),\end{aligned} \tag{2.24}$$

where $m$ is the mass of the atom, taken for all purposes as the mass of sodium. The effect of distortion of the waveform can be neglected, since the time of flight $T \sim \lambda_0/v \sim 10^{-10}\,\mathrm{s}$ combined with the transverse velocity dispersion $\Delta v_\perp = \frac{\hbar}{mw} \sim 0.4\,\mathrm{m/s}$ ($w = 8\,\mathrm{nm}$) results in an increase in width during propagation much smaller than the widths considered, $w \leq 100\,\mathrm{nm}$. This high collimation could be achieved through different experimental approaches, such as diffraction by a nanograting [59] and tight focusing techniques employed in atom lithography [111]. New perspectives in focusing procedures show that the widths of atomic beams $w \approx 8\,\mathrm{nm}$ might be achieved [111, 112].

The average of a function is taken along the coordinates transverse to the propagation, with a weight determined by $\psi_\perp$:

$$\bar{f}(y,z,...) := \int dydz f(y,z,...)|\psi_\perp(y,z)|^2. \tag{2.25}$$

The total phase $\phi(y,z,\Omega,v)$ is the sum of the quasistatic VdW phase $\phi^{\mathrm{vdW}}(y,z,v)$ and the QVSP $\phi^{\Omega}(y,z)$. Following the WKB approach from Refs. [57, 108] the observable phase is

$$\bar{\phi}(\Omega,v) = \mathrm{Arctan}\left[\frac{\overline{\sin\phi(\Omega,y,z,v)}}{\overline{\cos\phi(\Omega,x,z,v)}}\right]. \tag{2.26}$$

Increasing the sphere's angular velocity highlights the average QVSP as the component dependent on $\Omega$. Therefore, it is useful to define $\bar{\phi}^{\Omega}(\Omega,v) := \bar{\phi}(\Omega,v) - \bar{\phi}(0,v)$. Although $\phi^{\Omega}(x,z)$ is a geometric phase, the sum with a dynamic phase $\phi^{\mathrm{vdW}}$ combined with the trigonometric functions involved in the averaging process ends up bringing a velocity contribution to the average QVSP for finite-width wave packets.

Based on recent experimental advances with optically levitated nanoparticles, the sphere angular frequency used in numerical calculations is $\Omega = 2\pi \times 5\,\mathrm{GHz}$ [44]. Moreover,

the wave packets considered are gaussian beams centered on the edge of the sphere with longitudinal velocity $v$ and transverse width $w \leq 100\,\text{nm}$. In figure 2.5 $\bar{\phi}^{\Omega}(\Omega, v)$ is plotted in different configurations. Figure 2.5a shows $\bar{\phi}^{\Omega}$ as a function of the beam velocity for a nanosphere of radius $a = 50\,\text{nm}$. The width considered is $w = 100\,\text{nm}$. Fig. 2.5b presents $\bar{\phi}^{\Omega}(\Omega, v)$ versus $w$ for different velocities, considering $a = 35\,\text{nm}$. The plots show that the averaged QVSP tends to increase with velocity propagation and focusing, but specific values of width and velocity attenuate its value due to the vdW contribution. This effect can be mitigated by considering fast atomic beams with velocities comparable to $3\,\text{km/s}$ [59]. Figure 2.5b shows that $\bar{\phi}^{\Omega}(\Omega, v) \approx 0.1\,\text{mrad}$ for $w = 8\,\text{nm}$, a value close to the precision limit in current atom interferometry experiments [81, 113].

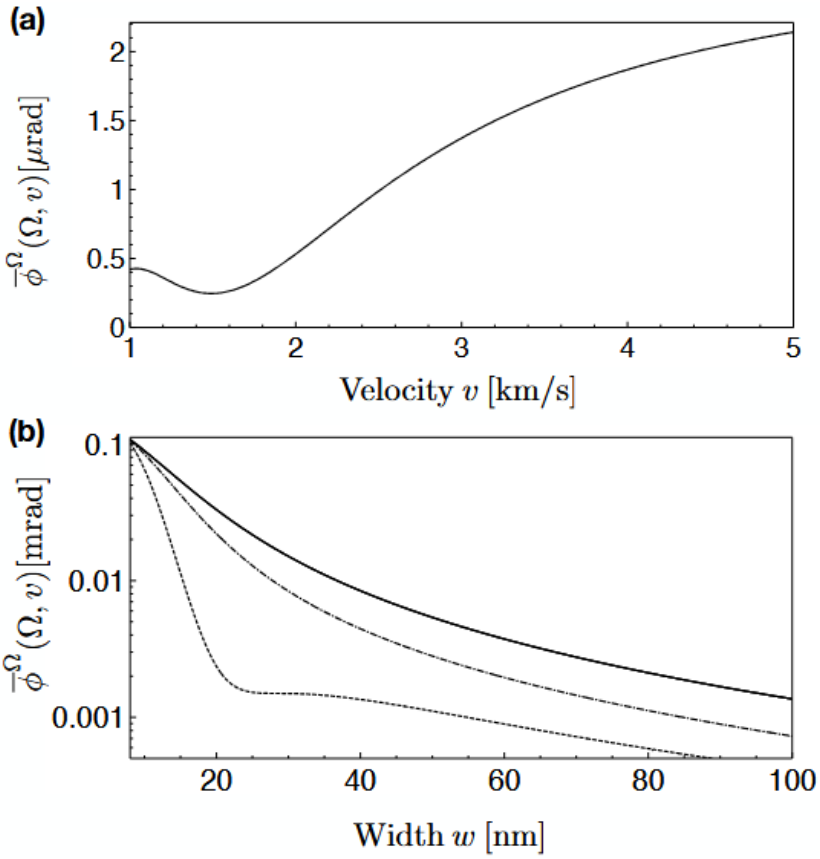


Figure 2.5: Figure from ref. [1]. Average QVSP for a gaussian atomic wave packets versus (a) velocity and (b) width of the beam. Parameters: (a)$a = 50\,\text{nm}$, $w = 100\,\text{nm}$. (b) $a = 35\,\text{nm}$, $v = 3\,\text{km/s}$ (dotted line), $v = 4\,\text{km/s}$ (dashed line) and $v = 5\,\text{km/s}$ (solid line). For both plots a 2-level Na atom and a potassium sphere rotating at $\Omega = 2\pi \times 5\,\text{GHz}$ are considered.

## 2.3 Quantum Vacuum Coriolis force

The relationship between the standard Sagnac effect and the ABE is well-understood theoretically. The similarity between the Lorentz and Coriolis forces [94] allows a rotating frame to mimic the presence of a magnetic field. This has been implemented in experiments, which used rotations to create effective artificial magnetic fields to trap clouds of neutral, ultra-cold gases [95]. Given the analogy between the two effects with the QVSP and the geometric nature of all phases cast as a circulation of effective potential [97, 98], one could expect that the force on the atom due to the rotating nanoparticle is similar to the Coriolis and Lorentz forces. In this section, the force on a moving ground-state 2-level atom due to the interaction with a nanoparticle is obtained using linear response theory. This result was derived by the author in collaboration with C. Villas-Bôas.

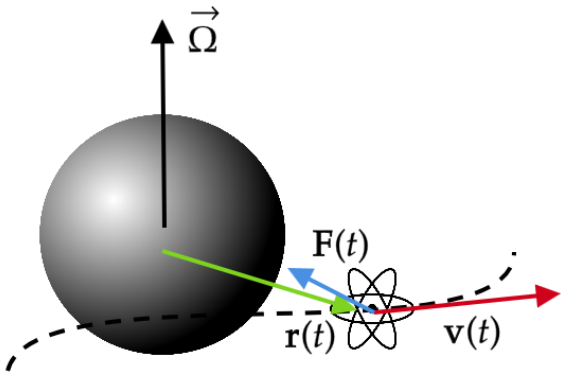


Figure 2.6: Representation of the force $\mathbf{F}$ by a rotating nanoparticle on a moving atom with velocity $\mathbf{v}$. The position of the atomic center of mass is $\mathbf{r}$.

The derivation starts with the expression of the force on an electric dipole due to the quantum electric field:

$$\mathbf{F}(t) = \nabla \frac{1}{2} \left\langle \mathbf{d}(t) \cdot \mathbf{E}(\mathbf{r}(t), t) \right\rangle , \tag{2.27}$$

with $\mathbf{r}(t)$ being the position of the atomic CM. The factor 1/2 follows from the fact that the atom has no permanent dipole, and the interaction is with a neutral, polarizable object [114]. As in the previous chapter, the average is over the initial state of the

atom+field system. Given the effect of induction of electric field and dipole, we can separate the total observables into a free evolving component and an induced one [56]

$$\begin{aligned}\mathbf{E}(\mathbf{r},t) &\approx \mathbf{E}^{\text{free}}(\mathbf{r}(t),t) + \mathbf{E}^{\text{ind}}(\mathbf{r}(t),t)\\ \mathbf{d}(t) &\approx \mathbf{d}^{\text{free}}(t) + \mathbf{d}^{\text{ind}}(t).\end{aligned} \tag{2.28}$$

In first order of induced dipole and field, the force is written as

$$\mathbf{F}(t) = \nabla\frac{1}{2}\left\langle \mathbf{d}^{\text{free}}(t)\cdot\mathbf{E}^{\text{ind}}(\mathbf{r}(t),t)\right\rangle + \frac{1}{2}\nabla\left\langle \mathbf{d}^{\text{ind}}(t)\cdot\mathbf{E}^{\text{free}}(\mathbf{r}(t),t)\right\rangle. \tag{2.29}$$

The induced observables are given in terms of response functions (see appendix A), namely

$$\mathbf{E}^{\text{ind}}(\mathbf{r}(t),t) = \int_{-\infty}^{t} d\tau \mathbf{G}^{R}(\mathbf{r}(t),\mathbf{r}(t-\tau),\tau)\cdot\mathbf{d}^{\text{free}}(t-\tau) \tag{2.30}$$

$$\mathbf{d}^{\text{ind}}(t) = \int_{-\infty}^{t} d\tau \boldsymbol{\alpha}^{A}(\tau)\cdot\mathbf{E}^{\text{free}}(\mathbf{r}(t-\tau),t-\tau). \tag{2.31}$$

Inserting Eqs. (2.30) and (2.31) in Eq. (2.29) results in terms in the form $\langle E_m^{\text{free}}(\mathbf{r},t)E_n^{\text{free}}(\mathbf{r}',t')\rangle$ and $\langle d_m^{\text{free}}(t)d_n^{\text{free}}(t')\rangle$. Those can be written in terms of the commutator and anticommutator, following the same procedure of chapter 1 (Eq. (1.14)). As a result, an expression analogous to Eq. (2.2) is obtained

$$\mathbf{F}(t) = \nabla_{\mathbf{r}}\frac{\hbar}{4}\int_{-\infty}^{t} d\tau[\mathcal{G}^{R}(\mathbf{r}(t),\mathbf{r}(t-\tau),\tau)g_{\mathbf{d}}^{H}(\tau) + \mathcal{G}_{\mathbf{E}}^{H,S}(\mathbf{r}(t),\mathbf{r}(t-\tau),\tau)\alpha^{A}(\tau)]. \tag{2.32}$$

The same approximations employed for the atomic motion in Sec. 2.1 are valid here. Within the VdW regime, the force in the stationary regime ($t \gg 1/\omega_0$) is

$$\mathbf{F}(t) = \nabla_{\mathbf{r}}\frac{i\hbar}{8\pi}\mathbf{v}(t)\cdot\nabla_{\mathbf{r}'}\int_{-\infty}^{\infty} d\omega\partial_{\omega}\delta\mathcal{G}^{R,S}(\mathbf{r},\mathbf{r}',\omega)g_{\mathbf{d}}^{H}(\omega)\Big|_{\mathbf{r}=\mathbf{r}'=\mathbf{r}(t)}, \tag{2.33}$$

where Plancherel's theorem has been used to change the integration in $\tau$ to $\omega$, theeqrefore converting the factor $\tau$ into a derivative in frequency. Applying the Fourier transform of Eq. (2.3) reduces Eq. (2.33) to

$$\mathbf{F}(t) = -\nabla_{\mathbf{r}}\frac{\hbar\alpha_0^{A}\omega_0}{4}\mathbf{v}(t)\cdot\nabla_{\mathbf{r}'}\partial_{\omega}\text{Im}[\delta\mathcal{G}^{R,S}(\mathbf{r},\mathbf{r}',\omega)]\Big|_{\mathbf{r}=\mathbf{r}'=\mathbf{r}(t)}. \tag{2.34}$$

Note that integrating the potential (in units of $\hbar$) $-\frac{\alpha_0^A \omega_0}{4}\mathbf{v}(t)\cdot\nabla_{\mathbf{r}'}\partial_\omega \mathrm{Im}[\delta\mathcal{G}^{R,S}(\mathbf{r},\mathbf{r}',\omega_0)]$ in time for a given atomic trajectory results in the local QVSP (Eq. (2.11)).

Using Eqs. (2.4), (2.5), and (2.8), the explicit calculation of that trace of the retarded Green's function and the derivatives leads to the final result of the force

$$\mathbf{F}(t) = -\frac{9}{4}\frac{\hbar\alpha_0^A\omega_0 \mathrm{Re}[\tilde{\alpha}''(\omega_0)]}{(4\pi\epsilon_0)^2 r^8(t)}\mathbf{v}(t)\times\mathbf{\Omega}. \tag{2.35}$$

Equation (2.35) resembles the Coriolis force acting on a particle with velocity $\mathbf{v}$ relative to a frame rotating with angular velocity $\mathbf{\Omega}$. This is a remarkable feature of the system, given that the force obtained here is with respect to an inertial frame.

For an estimation of the magnitude of the force, a sodium atom with velocity 5 km/s on a circular trajectory of radius $r = 10\,\mathrm{nm}$. For a potassium nanosphere of radius $a = 5\,\mathrm{nm}$ rotating at 5 GHz the force is $F \sim 10^{-19}\,\mathrm{N}$. Although very small, measurements of optical forces on single atoms reported magnitudes of the same order [115]. This finding allows for an analogy with the Mach principle, as the rotation of the nanoparticle mimics locally non-inertial effects [116].

# Chapter 3

# Dynamical Casimir photons from rotation of a nonspherical particle

The non-uniform motion of a neutral particle in the vacuum is radically different between quantum and classical electrodynamics viewpoints. In the latter, the emission of radiation by the particle requires any non-zero multipole moment. This is not true in the context of QED, as a moving particle can emit pairs of photons without prescribed multipoles due to the interaction with the quantum vacuum, a phenomenon known as the dynamical Casimir effect (DCE) [18–21, 85, 117].

Motivated by experiments with fast-rotating optically trapped non-spherical nanoparticles [2, 44, 45, 48], this chapter presents the derivation and discussion of the DCE by a rotating nanoparticle. The fast rotation beyond GHz could be a platform for an experimental measurement [45] of the quantum friction torque between a rotating particle and a surface [9, 53]. This leaves room for investigation of the DCE under those conditions, since high rotation frequencies could benefit the photon emission.

While the quantum friction for a spinning particle requires a dissipative medium [9,50,51,53,118,119], the photon emission from the DCE takes place due to the frequency modulation that arises from the rotation of a non-spherical particle, provided that the angular velocity is not parallel to any symmetry axis. The modulation causes field mode frequencies that are lower than twice the rotation angular frequency $\Omega$ to change sign,

leading to a Bogoliubov relation between the creation and annihilation operators of the corresponding modes [120–122], resulting in the emission of photons by mechanical motion. Naturally, the number of photons emitted during a given time interval increase with $\Omega$.

Given the smallness of the photon emission rate by the DCE under typical experimental conditions [85, 86, 122], a natural question is whether this effect could be measurable with new experiments with levitated nanoparticles. This chapter addresses this question by making a theory of the DCE for rotating particles. Although this problem has been already approached using a scalar field in 2+1 dimensions with Dirichlet boundary conditions for a perfect reflector [123], the derivation presented here takes into account the three-dimensional vectorial electromagnetic field and the dispersive behavior of the particle as well. In addition, the optimization of the effect is shown by tuning the rotation frequency near the GHz polaritonic resonance of a barium strontium titanate (BST) nanoparticle [9, 124, 125]. As an application, the photon emission rate is calculated for a spheroid rotating perpendicular to its symmetry axis. In that case, the eccentricity optimizing the emission is non-trivial. An analytical discussion for DCE in metals is also presented.

Section 3.1 presents the derivation of the emission spectrum by establishing the Bogoliubov relations through the scattering of the quantum electric field by a rotating particle. In the following section 3.2, numerical plots are shown for the photon emission rate as a function of the shape and size of a nanospheroid.

## 3.1 Dynamical Casimir effect frequency spectrum for a spinning particle

### 3.1.1 Bogoliubov relation in the dipolar regime

Following a scattering approach, the system is modeled as a neutral rotating particle with angular velocity $\boldsymbol{\Omega} = \Omega\hat{\mathbf{z}}$ ($\Omega > 0$) within the dipole approximation. The electric

dipole induced by the quantum field is $\mathbf{d}(\omega)$ and is $\Omega$-dependent (see appendix B). The particle is located at the origin of the coordinate system. Given that the particle rotates for a given window of time $T$, the output electric field (free quantum field for $t \to \infty$) is different from the input field (free field at $t \to -\infty$) by a dipole field. The relation between fields is [122]

$$\mathbf{E}_{\text{out}}(\mathbf{r},\omega) = \mathbf{G}(\mathbf{r},\mathbf{r}'=0,\omega)\cdot\mathbf{d}(\omega) + \mathbf{E}_{\text{in}}(\mathbf{r},\omega), \tag{3.1}$$

with $\mathbf{G} = \mathbf{G}^R - \mathbf{G}^A$ being the difference between the retarded and advanced Green's functions. Taking the radiation zone limit ($\omega r/c \gg 1$), its expression is

$$\mathbf{G}(\mathbf{r},\mathbf{r}'=0,\omega) = \frac{2i\omega^2 \sin\left(\frac{\omega r}{c}\right)}{4\pi\epsilon_0 c^2 r}\left[\mathbb{1} - \frac{\mathbf{r}\otimes\mathbf{r}}{r^2}\right]. \tag{3.2}$$

Since the scatterer is localized, a convenient choice is to write the input and output fields in the multipole spherical wave basis (see appendix D), for which the expression is [91, 126]

$$\mathbf{E}_{\text{in(out)}}(\mathbf{r},\omega) = i\mathcal{E}(\omega)\sum_{j=1}^{\infty}\sum_{m=-j}^{j}\sum_{\lambda=\text{E,M}} a_{jm\lambda}^{\text{in(out)}}(\omega)\theta(\omega)\mathbf{I}_{jm\lambda}(\mathbf{r},\omega) - a_{jm\lambda}^{\text{in(out)}\dagger}(-\omega)\theta(-\omega)\mathbf{I}_{jm\lambda}^{*}(\mathbf{r},\omega). \tag{3.3}$$

Here, $\mathcal{E}(\omega) = \sqrt{\frac{\hbar\omega}{2\epsilon_0 c}}$ is the mode amplitude and the modes are labeled by the quantum numbers $j$, $m$ and $\lambda$: $j$ represents the order of the multipole and the total angular momentum of the wave, $m$ is the eigenvalue for the z-component of the angular momentum and $\lambda$ labels the polarization of the wave, indicating whether the multipole is electric (E) or magnetic (M). The operators $a_{jm\lambda}^{\text{in(out)}}(\omega)$ and $a_{jm\lambda}^{\text{in(out)}\dagger}(\omega)$ are the annihilation and creation operators, respectively. By the quantization process, they obey the relation

$$[a_{jm\lambda}^{\text{in(out)}}(\omega), a_{j'm'\lambda'}^{\text{in(out)}\dagger}(\omega')] = \delta(\omega-\omega')\delta_{jj'}\delta_{mm'}\delta_{\lambda\lambda'}. \tag{3.4}$$

Furthermore, $\mathbf{I}_{jm\lambda}(\mathbf{r},\omega)$ are the vector spherical harmonics [91]. Since no magnetic effects are considered, the discussion henceforth shall take into account only the modes related

to electric multipoles ($\lambda = \mathrm{E}$). The asymptotic expression for $\mathbf{I}_{jm\mathrm{E}}(\mathbf{r},\omega)$ in the radiation zone is

$$\mathbf{I}_{jm\mathrm{E}}(\mathbf{r},\omega) \approx \frac{4\pi i^{j-1}}{\sqrt{j(j+1)}} \frac{\cos\left(\frac{\omega r}{c} - j\frac{\pi}{2}\right)}{r} \nabla_{\hat{\mathbf{r}}} Y_{jm}(\hat{\mathbf{r}}), \tag{3.5}$$

where $Y_{jm}(\hat{\mathbf{r}})$ denotes the spherical harmonics and $\nabla_{\hat{\mathbf{r}}}$ is the gradient with respect to the angular coordinates.

By combining Eqs. (3.5), (3.3), and (3.2) with Eq. (3.1), it is possible to obtain a Bogoliubov relation between the input and output field operators through the dipole operator of the rotating particle:

$$\begin{aligned} a^{\mathrm{out}}_{10\mathrm{E}}(\omega) &= \frac{\omega^2}{2\sqrt{6}\pi^{3/2}\epsilon_0 c^2 \mathcal{E}(\omega)} d_z(\omega) + a^{\mathrm{in}}_{10\mathrm{E}}(\omega) \\ a^{\mathrm{out}}_{1\pm1\mathrm{E}}(\omega) &= \mp \frac{\omega^2}{4\sqrt{3}\pi^{3/2}\epsilon_0 c^2 \mathcal{E}(\omega)} (d_x(\omega) \mp i d_y(\omega)) + a^{\mathrm{in}}_{1\pm1\mathrm{E}}(\omega). \end{aligned} \tag{3.6}$$

### 3.1.2 Spectrum and total emission rate

The number of photons emitted with frequencies between $\omega$ and $\omega + d\omega$ in the mode $jm\mathrm{E}$ per unit of time is

$$d\Gamma_{jmE} = \frac{1}{T} \langle 0_{in}|\, a^{out\dagger}_{jmE}(\omega) a^{out}_{jmE}(\omega)\, |0_{in}\rangle\, d\omega, \tag{3.7}$$

with $T$ being the total rotation time. Based on Eq. (3.6), the only contributions are from $j = 1$ and $m = 0, \pm 1$. To calculate the expected values using Eq. (3.6), explicit expressions for the induced dipole are needed. Using an approach inspired by the derivation of Ref. [50], it is possible to show that the dipole of a particle rotating perpendicular to its symmetry axis in terms of its polarizability is (see Appendix B)

$$\mathbf{d}(\omega) = \boldsymbol{\alpha}_0(\omega) \cdot \mathbf{E}_{\mathrm{in}}(\mathbf{0},\omega) + \boldsymbol{\alpha}_+(\omega) \cdot \mathbf{E}_{\mathrm{in}}(\mathbf{0},\omega + 2\Omega) + \boldsymbol{\alpha}_-(\omega) \cdot \mathbf{E}_{\mathrm{in}}(\mathbf{0},\omega - 2\Omega). \tag{3.8}$$

Here, the modulation in frequency of the electric field's modes by the rotation frequency is explicit. The sidebands occur as a result of the discrete time translation symmetry with half of the period of the particle rotation, and hence the modulation with $2\Omega$. As

mentioned above, for low frequency ($< 2\Omega$) modes, the output creation operators become dependent on the input annihilation ones and vice versa. The tensor polarizabilities $\boldsymbol{\alpha}_0(\omega)$, $\boldsymbol{\alpha}_+(\omega)$, and $\boldsymbol{\alpha}_-(\omega)$ are defined by

$$\begin{aligned}
\boldsymbol{\alpha}_0(\omega) &= \begin{pmatrix} \frac{1}{2}(S^+ + S^-) & \frac{i}{2}(S^+ - S^-) & 0 \\ \frac{-i}{2}(S^+ - S^-) & \frac{1}{2}(S^+ + S^-) & 0 \\ 0 & 0 & \alpha_\perp(\omega) \end{pmatrix} \\
\boldsymbol{\alpha}_+(\omega) &= \begin{pmatrix} \frac{\Delta^+}{2} & \frac{-i\Delta^+}{2} & 0 \\ \frac{-i\Delta^+}{2} & \frac{-\Delta^+}{2} & 0 \\ 0 & 0 & 0 \end{pmatrix} \\
\boldsymbol{\alpha}_-(\omega) &= \begin{pmatrix} \frac{\Delta^-}{2} & \frac{i\Delta^-}{2} & 0 \\ \frac{i\Delta^-}{2} & \frac{-\Delta^-}{2} & 0 \\ 0 & 0 & 0 \end{pmatrix}.
\end{aligned} \tag{3.9}$$

The superscripts $\pm$ indicate the positive $(\omega + \Omega)$ or negative $(\omega - \Omega)$ Doppler-shifted frequencies at which the mean polarizability $S(\omega)$ and difference $\Delta(\omega)$ are taken:

$$\begin{aligned}
S(\omega) &= \frac{\alpha_\parallel(\omega) + \alpha_\perp(\omega)}{2} \\
\Delta(\omega) &= \frac{\alpha_\parallel(\omega) - \alpha_\perp(\omega)}{2},
\end{aligned} \tag{3.10}$$

where $\alpha_\perp(\omega)$ and $\alpha_\parallel(\omega)$ are the polarizabilities in a direction perpendicular and parallel to the particle's symmetry axis, respectively. It is assumed that the particle has a symmetry axis, and thus the eigenvalue $\alpha_\perp(\omega)$ of the polarizability tensor of the particle at rest is degenerate.

In order to compute the photon emission rate, one can define the correlation matrix

$$C_{lm} = \langle 0_{in}| \, d_l^\dagger(\omega) d_m(\omega) \, |0_{in}\rangle \,, \tag{3.11}$$

in terms of which Eq. (3.7) combined with (3.6) becomes

$$\begin{aligned}
\frac{d\Gamma_{10}}{d\omega} &= \frac{1}{12\pi^3} \frac{\omega^3}{\hbar c^3 \epsilon_0} C_{zz} \\
\frac{d\Gamma_{1\pm1}}{d\omega} &= \frac{1}{48\pi^3} \frac{\omega^3}{\hbar c^3 \epsilon_0} [C_{xx} + C_{yy} \pm i(C_{yx} - C_{xy})].
\end{aligned} \tag{3.12}$$

Using the explicit expression for the dipole (Eq. (3.8)), it follows that no photons are emitted in the modes $m = 0, -1$. As expected by the conservation of the angular momentum, the photons must be in the mode $m = 1$, since, by construction, the particle's

angular momentum is along the positive z-axis. Therefore, the emission spectrum is

$$d\Gamma_{11} = \frac{|\omega - 2\Omega|^3 \omega^3 |\Delta(\omega - \Omega)|^2 \Theta(2\Omega - \omega)}{36\pi^3 c^6 \epsilon_0^2} d\omega. \tag{3.13}$$

Given that only one angular momentum eigenstate contributes, the mode subscript will be dropped hereafter.

The total number of photons emitted per unit of time is obtained by integrating the spectrum (Eq. (3.13)) over all frequencies. Naturally, only frequencies $< 2\Omega$ contribute to the effect. The photon emission rate is thus

$$\Gamma(\Omega) = \frac{1}{144\pi^3 c^6 \epsilon_0^2} \int_0^{2\Omega} d\omega \omega^3 |\omega - 2\Omega|^3 |\Delta(\omega - \Omega)|^2. \tag{3.14}$$

This is the central result of this chapter. It allows for the calculation of the photon emission rate for any cylindrically symmetric isotropic rotating object in the dipole approximation. The difference between polarizabilities $\Delta(\omega)$ contains the information of the material and geometry of the particle.

As a first application of equation (3.14), one can compute the photon emission rate for a non-dispersive rotating particle. In practice, this regime can be achieved when the rotation frequency is much lower than the typical frequencies at which the dispersive behavior of the material becomes relevant. In that case, $\Delta(\omega)$ assumes approximately its quasistatic value $\Delta(0)$. Hence, equation (3.14) becomes

$$\Gamma_{QS} = \frac{\Omega^7}{\omega_{QS}^6}, \tag{3.15}$$

where the characteristic frequency $\omega_{qs}$ is defined by

$$\omega_{QS} = \left( \frac{315\pi^3 c^6 \epsilon_0^2}{2|\Delta(0)|^2} \right)^{1/6}. \tag{3.16}$$

The dependence of the photon emission on $\Omega^7$ is illustrative of the modulation mechanism of the DCE mentioned earlier. It is illustrative to compare with other dynamical Casimir systems. Interesting examples are the DCE emission rate for an oscillating mirror, that

scales with $\Omega^5$ if the transverse dimension is bigger than the wavelength $2\pi c/\Omega$ [122, 127, 128], but the scaling with $\Omega$ changes if the transverse length is smaller than $2\pi c/\Omega$, leading to a photon emission rate that increases with $\Omega^9$ [39]. The same dependence in $\Omega^9$ is obtained for an oscillating ground-state atom [33] and an oscillating sphere [129].

## 3.2 Applications

### 3.2.1 Perfectly-conducting nanodumbbell

Ref. [44] reports that a rotation frequency of 5.2 GHz was achieved for a dumbbell-shaped nanoparticle (see figure 3.1), motivating the application of expression ((3.14)) for this geometry to estimate the effect under typical experimental conditions. If the material is not dispersive, which is the case for a perfect conductor, the emission rate is given by Eq. (3.15). From Ref. [130], the difference in the polarizabilities $\Delta(0)$ for a perfectly conducting dumbbell is $\Delta = 10\pi\epsilon_0\zeta(3)R^3$, where $R$ is the radius of each sphere that constitutes the dumbbell, and $\zeta(x)$ is Riemann's zeta function. Thus, the photon emission rate is

$$\Gamma = \frac{40\zeta^2(3)}{63\pi}\left(\frac{\Omega R}{c}\right)^6 \Omega. \tag{3.17}$$

Following the experiment presented in reference [44], the experimental values for $R$ and $\Omega$ are $\Omega = 2\pi \times 5.2\,\mathrm{GHz}$ and $R = 150\,\mathrm{nm}$. Under these conditions, the emission rate is $\Gamma \sim 6 \times 10^{-19}\,\mathrm{s}^{-1}$, indicating a very small effect. Note that this number overestimates the photon emission under experimental conditions, since we considered a perfect reflector, while experiments used silica nanoparticles. [2, 44, 48].

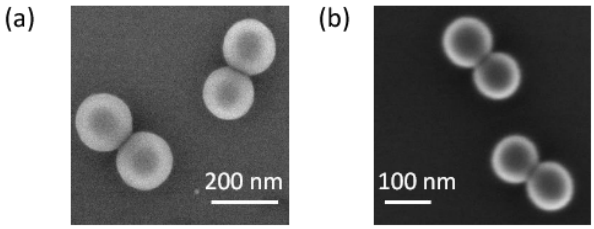


Figure 3.1: Silica nanodumbbells of different sizes. The scale bar in (a) is 200 nm and 100 nm in (b). Figure adapted from Ref. [2].

Note that the experimental parameters are such that $\Omega R = 4.9\times10^3\,\mathrm{m/s}$, which is close to the speed of sound in amorphous silica $v_{\mathrm{sound}} \sim 6.0\times10^3\,\mathrm{m/s}$ [131] and could represent the speed limit before breaking the solid material. Now, we take new values of frequency and radius such that $\Omega' R' = 4.9\times10^3\,\mathrm{m/s}$ as before and the smallest possible value of $R'$ still compatible with our approach based on the macroscopic Maxwell equations: $R' = 1\,\mathrm{nm}$. In this case, we find $\Omega' = 2\pi\times 0.78\,\mathrm{THz}$ and $\Gamma' = 150\,\Gamma = 10^{-16}\,\mathrm{s}^{-1}$ which is still very small. To enhance the effect, it is possible to explore plasmonic or polaritonic resonances, and therefore, the frequency dependency of $\Delta$ must be considered. This will be done with spheroids, which allow for analytical expressions for the dispersive polarizability.

### 3.2.2 Spheroids

For a prolate spheroid with radii $r_\perp$ and $r_\parallel$, with $r_\parallel > r_\perp$ (see Figure 3.2), the difference $\Delta(\omega)$ between transverse $\alpha_\perp(\omega)$ and longitudinal $\alpha_\parallel(\omega)$ is given by [132]

$$\Delta(\omega) = 4\pi\epsilon_0 \frac{r_\parallel r_\perp^2}{6}\left(\frac{1}{N_\parallel}-\frac{1}{N_\perp}\right)\frac{(\epsilon(\omega)-1)^2}{(\epsilon(\omega)-1+1/N_\parallel)(\epsilon(\omega)-1+1/N_\perp)}, \tag{3.18}$$

where $\epsilon(\omega)$ is the dielectric function of the material and $N_\perp$ and $N_\parallel$ are the depolarization factors, which are geometric, dimensionless constants given by

$$N_i = \frac{r_\parallel r_\perp^2}{2}\int_0^\infty \frac{ds}{(s+r_i^2)(s+r_\perp^2)\sqrt{s+r_\parallel^2}},\ i = \perp, \parallel . \tag{3.19}$$

For a sphere, one has $N_\perp = N_\parallel = 1/3$. In the case of interest of a prolate spheroid, the depolarization factors are given by elementary functions of the eccentricity $e := \sqrt{1 - \frac{r_\perp^2}{r_\parallel^2}}$ :

$$\begin{aligned} N_\parallel &= \frac{1-e^2}{2e^3}\left(\log\frac{1+e}{1-e} - 2e\right) \\ N_\perp &= \frac{1}{2}(1 - N_\parallel). \end{aligned} \tag{3.20}$$

Because the behavior of the dielectric function changes with the nature of the particle material, the discussion of the DCE for a rotating spheroid will be divided into metals and dielectrics.

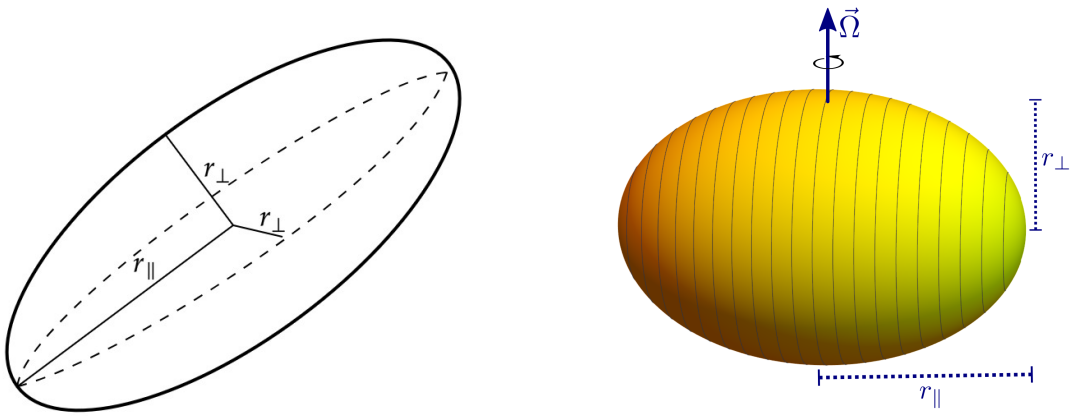


(a) (b)

Figure 3.2: (a) Representation of a prolate spheroid indicating the radii $r_\parallel$ and $r_\perp$ along the symmetry axis and perperdincular to it, respectively. (b) 3-dimensional scheme of a rotating prolate spheroid.

**Metals**

For metals, we take the Drude model (2.22) for the dielectric function, namely

$$\epsilon(\omega) = 1 - \frac{\omega_p^2}{\omega(\omega + i\gamma)}, \tag{3.21}$$

where $\omega_p$ is the plasma frequency and $\gamma$ the inverse relaxation time, properties of the material. Note that $\omega \to 0$ implies in $\epsilon(\omega) \to \infty$, and thus Eq. (3.18) becomes

$$\Delta(0) = 4\pi\epsilon_0 \frac{r_\parallel r_\perp^2}{6}\left(\frac{1}{N_\parallel} - \frac{1}{N_\perp}\right). \tag{3.22}$$

This corresponds to the perfect reflector regime, which occurs when $\Omega \ll \omega_p$. Defining $\Gamma_0$ as the photon emission rate for a perfectly reflecting metallic spheroid, we use Eqs. (3.15) and (3.22) to obtain:

$$\Gamma_0 = \frac{\Omega^7}{\omega_0^6}, \tag{3.23}$$

with $\omega_0$ defined by

$$\omega_0 := \left[ \frac{2835\pi c^6}{8(r_\parallel r_\perp^2)^2 \left(\frac{1}{N_\parallel} - \frac{1}{N_\perp}\right)^2} \right]^{1/6}. \tag{3.24}$$

The inclusion of the dispersive behavior of the emitter in the photon emission rate (Eq. (3.14)) allows for an analytical approach. Combining Eqs. (3.18) and (3.21) into (3.14) results in

$$\Gamma = \frac{35}{16}\frac{\Omega^7}{\omega_0^6}\int_0^1 du(1-u^2)^3 \frac{1}{\left[\left(1-\frac{\Omega^2u^2}{\omega_p^2 N_\perp}\right)^2 + \left(\frac{\Omega\gamma u}{\omega_p^2 N_\perp}\right)^2\right]\left[\left(1-\frac{\Omega^2u^2}{\omega_p^2 N_\parallel}\right)^2 + \left(\frac{\Omega\gamma u}{\omega_p^2 N_\parallel}\right)^2\right]}, \tag{3.25}$$

where the dimensionless variable $u := \frac{\Omega-\omega}{\Omega}$ was introduced in the integral. If $\omega_p \gg \Omega$, the emission peaks determined by the integrand denominator lie outside the integration region, resulting in an emission spectrum independent of the dispersive behavior of $\Delta(\omega)$. As expected, the corresponding emission rate is $\Gamma_0$ since it corresponds to the perfect reflector approximation.

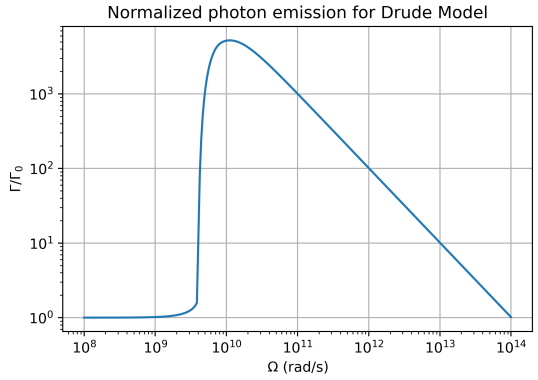


Figure 3.3: Photon emission for a metal with $\omega_p = 10^{10}$ rad/s and $\gamma = 10^{-4}\omega_p$ as a function of the rotation frequency. Geometric parameters for the plot: $N_\perp = 0.15$, $N_\parallel = 0.7$, $r_\parallel = 2r_\perp = 2\,\text{nm}$. The peak in the plot corresponds to an emission rate of $\Gamma \approx 10^{-32}\,\text{s}^{-1}$.

The scaling of $\Gamma$ with $\Omega$ changes if $\Omega \sim \omega_p$, the resonant regime (see Fig. 3.3). This can be shown by making a lorentzian approximation: since typically $\omega_p \gg \gamma$, the points that contribute to the integral are the ones near the two sharp emission peaks (see Fig. 3.4) of width $\sim \gamma/\omega_p \ll 1$, located at the points $u_i = \omega_p\sqrt{N_i}/\Omega$. Hence, the spectrum is constant on those values, except for terms involving $1/(1 - \Omega u/\omega_p N_i)$. The complete expression becomes the sum of two peaks, each representing a plasmon resonance associated with a depolarization factor. The emission rate is thus

$$\Gamma = \frac{35\pi}{16}\frac{\Omega^6\omega_p^2}{\omega_0^6\gamma}\left\{N_\perp \frac{(1-u_\perp^2)^3}{\left(1-\frac{u_\perp^2}{u_\parallel^2}\right)^2 + \frac{\gamma^2 N_\perp}{\omega_p^2 N_\parallel^2}} + N_\parallel \frac{(1-u_\parallel^2)^3}{\left(1-\frac{u_\parallel^2}{u_\perp^2}\right)^2 + \frac{\gamma^2 N_\parallel}{\omega_p^2 N_\perp^2}}\right\}. \tag{3.26}$$

If the shape of the spheroid is close to a sphere in such a way that $N_\parallel \approx N_\perp$, which is referred to as the quasi-degenerate regime, instead of two lorenztian peaks, the spectrum is given by a single squared lorentzian distribution, leading to

$$\Gamma = \frac{35\pi}{64}\frac{\Omega^6\omega_p^4}{\omega_0^6\gamma^3}N_\perp^2(1-u_\perp^2)^3. \tag{3.27}$$

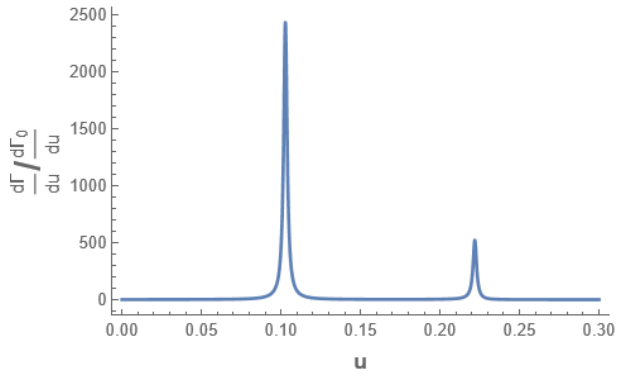


Figure 3.4: Emission spectrum for a metallic spheroid normalized by the quasistatic spectrum. Parameters for the plot: $\Omega = 2\pi \times 6 \times 10^9$ rad/s, $\omega_p = 10^{10}$ rad/s, $\gamma = 10^8$ rad/s, $r_\parallel = 2r_\perp = 2\,\text{nm}$, $N_\perp = 0.15$, and $N_\parallel = 0.7$. Smaller $\gamma/\omega_p$ ratios results in sharper peaks. Analytically, the peaks are located at the points $u_\perp = 0.10$ and $u_\parallel = 0.22$.

Equation (3.26) is valid as long $\Omega \gtrsim \omega_p$. Beyond the resonant regime, on which $\Omega \gg \omega_p$

(high-frequency limit), Eq. 3.26 becomes

$$\Gamma = \frac{35\pi}{16}\frac{\Omega^6\omega_p^2}{\omega_0^6\gamma}\left[\frac{N_\perp}{\left(1-\frac{u_\perp^2}{u_\parallel^2}\right)^2+\frac{\gamma^2 N_\perp}{\omega_p^2 N_\parallel^2}}+\frac{N_\parallel}{\left(1-\frac{u_\parallel^2}{u_\perp^2}\right)^2+\frac{\gamma^2 N_\parallel}{\omega_p^2 N_\perp^2}}\right]. \tag{3.28}$$

Note that the term in brackets does not depend on $\Omega$ and thus the DCE emission rate scales with $\Omega^6$, instead of the $\Omega^7$ factor of the quasistatic regime. Figure 3.3 shows the photon emission rate normalized by $\Gamma_0$ as a function of $\Omega$ by integrating Eq. (3.25) numerically. Due to the plasmonic resonance the the photon emission rate increases in over 3 orders of magnitude relative to the quasistatic regime. Past the resonance at the plasma frequency considered, the graph decays with $1/\Omega$, validating the analytical predictions. The same behavior is observed for dielectrics, as is shown in the next section.

As a final remark regarding metals, note that the optical parameters used in figure 3.3 are not realistic. Most metals have much higher plasma frequencies, in a way that typical experimental rotation frequencies lie in the quasistatic regime. In addition, the $\gamma/\omega_p$ ration This difficulty can be overcome with dielectrics, as some dielectric materials have polaritonic resonance frequencies in the GHz range.

**Dielectrics**

The permittivity of dielectrics can be described by the Lorentz model for many materials. When considering a single oscillator, the Lorentz model can be written in the form

$$\epsilon(\omega) = \epsilon(\infty) + \frac{\epsilon(0)-\epsilon(\infty)}{1+(\omega/\omega_T)^2+i\omega\gamma/\omega_T^2}, \tag{3.29}$$

where $\epsilon(0)$ and $\epsilon(\infty)$ are the dielectric functions at low and high frequencies, respectively, and $\omega_T$ is the oscillator resonance frequency, which dictates the order of the polaritonic resonance frequency if $\omega_T \gg \gamma$. In order for the mechanical motion to excite polaritonic modes, it is necessary that $\Omega \sim \omega_T$. This match occurs for the barium strontium titanate (BST) material, considering the current experimental rotation frequencies. The Lorentz

model parameters for BST are $\epsilon(0) = 7.1$, $\epsilon(\infty) = 2.896$, $\gamma = 2.8 \times 10^8\,\mathrm{rad/s}$ and $\omega_T = 5.7 \times 10^9\,\mathrm{rad/s}$ [9]. If $\Omega \ll \omega_T$, the emission rate is in the quasistatic regime. Therefore, Eq. (3.15) can be rewritten in terms of the polaritonic resonance frequency $\omega_T$:

$$\Gamma_{QS}(\Omega) = \mathcal{C}_{QS} \left(\frac{\Omega}{\omega_T}\right)^7, \tag{3.30}$$

with $\mathcal{C}_{QS} = 3.9764 \times 10^{-39}\,\mathrm{s}^{-1}$. The spectrum plot (figure 3.5) and the numerical evaluation of the photon emission rate (figure 3.6) are shown below for a spheroid of radius $r_\parallel = 2r_\perp = 2\,\mathrm{nm}$ and eccentricity $e = 0.866$.

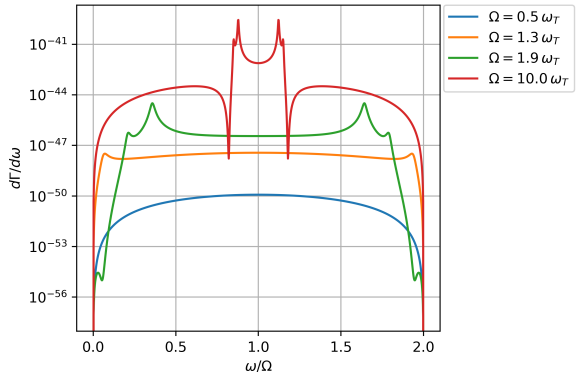


Figure 3.5: BST emission spectrum for five different rotation frequencies $\Omega$.

From figure 3.5, one can see the transition from the low-frequency regime ($\omega \ll \omega_T$), represented by the blue curve, to the high-frequency behavior ($\omega \gg \omega_T$), represented by the red curve. In the former case, the spectrum is a sixth-order polynomial that results from neglecting the frequency dependence of $\Delta(\omega)$ in Eq. (3.13). The latter is dominated by the two (or four, if examined closely) resonant frequency peaks.

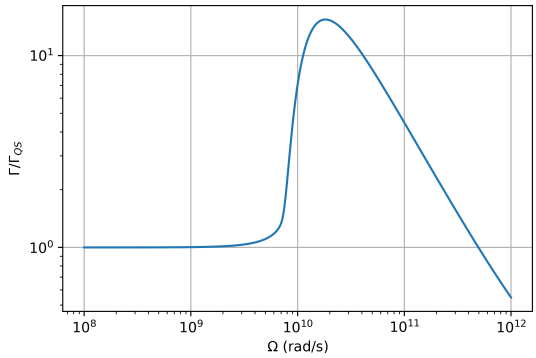


Figure 3.6: Emission rate for the BST normalized by the low-frequency (quasi-static) emission rate $\Gamma_{QS}$.

The numerical integration of the spectrum shown in Fig. 3.5 leads to the total emission rate for a BST spheroid. We plot the emission rate versus rotation frequency in Fig. 3.6. As expected, when $\Omega \sim \omega_T$ the normalized emission reaches its maximum, which is more than 10 times larger than the quasi-static result. Past the resonance, $\Omega \gg \omega_T$, an analysis of the curve slope shows that $\Gamma \sim \Omega^6$, as in the case of metals.

### 3.2.3 Optimization of the particle shape

All calculations to this point consider a nanoparticle with a fixed radius. In this section, in order to optimize the effect, we consider instead a fixed value for the linear velocity of the tip of the particle. Indeed, the maximum achievable rotational frequency (bursting frequency) before fracturing is determined by an upper bound for the linear velocity, which in its turns is given in terms of the ultimate tensile strength of the material [47]. The role of geometry is then studied by calculating the emission rate as a function of the size and shape (eccentricy) of the spheroid, for a fixed linear velocity of the tip.

The maximum velocities of rotating nanoparticles in experiments [44, 47] are close to the speed of sound in the materials used, suggesting that this velocity could approximate the bursting limit. Therefore, taking the velocity of the tip of the spheroid as the speed

of sound gives the constraint for the angular frequency

$$\Omega = \frac{v_s}{r_\parallel}, \tag{3.31}$$

with $v_s$ denoting the sound velocity of the material. For BST, $v_s \approx 8 \times 10^3\,\mathrm{m/s}$ [133]. Given those constraints, we plot the photon emission rate as a function of the longitudinal radius $r_\parallel$ (figure 3.7) and of the eccentricity $e$ (figure 3.8).

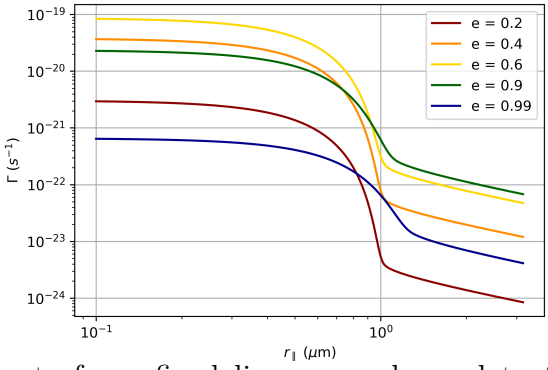


Figure 3.7: Emission rate for a fixed linear speed equal to the speed of sound of the material $v_s = \Omega r_\parallel = 8 \times 10^3\,\mathrm{m/s}$, for four different shapes characterized by the eccentricity $e$. The small values of $r_\parallel$ correspond to the high-frequency domain ($\Omega \gg \omega_T$), and vice versa.

The plot in figure 3.7 indicates that the eccentricity optimizing the emission depends on the regime of rotation, which is expected since the scaling with $\Omega$ changes, and so does the dependence in $r_\parallel$. One could expect the emission rate to increase with $r_\parallel$, given that $\Gamma$ scales with the squared volume. [1] However, this is not the case, since the constraint (Eq. 3.31) imposes that $\Omega$ decreases with the radius, and therefore $\Gamma$ also decreases for $r_\parallel \gg v_s/\omega_T$.

[1] The emission rate depends on $|\Delta(\omega)|^2$ and $\Delta(\omega)$ is proportional to the volume of the particle, as shown by Eq. 3.18.

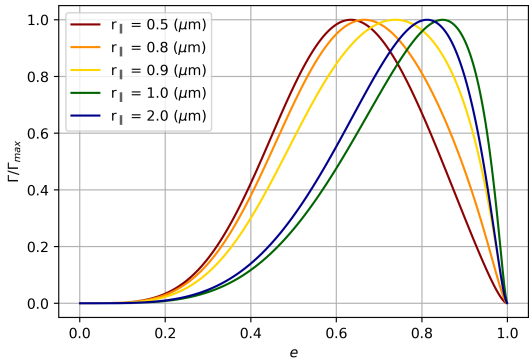


Figure 3.8: Emission rate as a function of the eccentricity $e$ for different $r_{\parallel}$ values at fixed linear speed, equal to the material's sound speed $v_s = \Omega r_{\parallel} = 8 \times 10^3\,\mathrm{m/s}$. Each curve is normalized by its maximum value. The red curve (largest $r_{\parallel}$) corresponds to the high-frequency domain ($\Omega \gg \Omega_T$), while smaller $r_{\parallel}$ values represent the low-frequency regime. Intermediate curves demonstrate the transition across the resonance range. As expected, the spherical case ($e = 0$) shows zero emission.

The optimal eccentricity for a given $r_{\parallel}$ is neither a perfect sphere (as expected) nor a spheroid with $e \to 1$ ($r_{\parallel} \gg r_{\perp}$), but a value in between. This can be seen in Fig. 3.8, in which $\Gamma(e)$ is shown for different values of $r_{\parallel}$, ranging from high to low frequency regimes. Each size has its optimal eccentricity, and this dependence is non-trivial.

# Conclusions and final remarks

This thesis investigated effects of rotations in the interaction between a particle and the quantum electromagnetic field in its vacuum state. This was done through the computation of the atom interferometer phase induced by a rotating nanoparticle, and the calculation and analysis of the photon emission rate by a spinning particle. Although a theoretical study, all the results presented were based on realistic experimental parameters.

Chapter 1 reviewed the theory of open quantum systems for atom interferometers, which allows for the calculation of the phases and decoherence emerging from interactions with the environment during atom propagation. In second order of perturbation theory, the phase is the sum of contributions involving a single interferometer path (local, usual to quantum optics) or both paths combined (non-local). For a moving atom in the ground state interacting with a neutral object, the phase associated with the Casimir interaction arises from the scattering by the surface of virtual photons emitted from the atom. In this context, the nonlocal phase is an observable manifestation of the emission of a virtual photon in a given path and absorption of the scattered photon in another path. Both local and non-local terms can be written as a sum of phases induced by quantum fluctuations of the atomic dipole and field.

In chapter 2, the formalism developed in chapter 1 was applied to derive the quantum vacuum Sagnac phase, a phase induced on the CM degree of freedom of an atom in its ground state by a neutral spinning nanoparticle in the vicinity. The phase arises from the atomic motion during the emission and absorption of virtual photons scattered by

the nanoparticle. Moreover, the phase is proven to be a geometric Berry phase analogous to the Aharonov-Bohm effect, as the phase carries information about rotation in a localized region of space mimicking a noninertial frame, while the propagation is described with respect to an inertial frame. If the atomic transition frequency is close to the plasmonic resonance, the experimentally accessible quantum vacuum Sagnac phase for Gaussian wavepackets is close to the sensitivity limit of current atom interferometers. The dispersive force on the moving atom by a spinning nanosphere is calculated, and the result is proportional to the cross product between the atom velocity and the sphere's angular frequency, similar to the Coriolis force.

Chapter 3 continued the study of rotations in the context of quantum vacuum interactions by analyzing the photon emission rate by a rotating non-spherical nanoparticle. Describing the scattering of the quantum electric field by the spinning particle results in a Bogoliubov relation between the field operators before and after the interaction with the particle. This relation is mediated by the induced dipole of the particle, which carries information on the modulation in frequency of the field modes by the rotation. The emission spectrum was obtained for metallic and dielectric spheroids, and in both cases the emission was shown to be greatly enhanced when the rotation frequency approaches plasmonic or polaritonic resonances. Given the proximity of current experimental rotation frequencies to BST's polaritonic resonances, this material was considered for the study of the emission rate under realistic experimental conditions. The role of geometry was analyzed, and numerical plots showed the non-trivial dependence of the emission rate on the radius and eccentricity of the spheroidal particle.

The results presented in this thesis leave room for further research. The photon emission rate by the dynamical Casimir effect with rotating nanoparticles can be investigated in the context of the emitter near a surface, which has been recently implemented experimentally [45], but, to the knowledge of the author, has not been theoretically approached so far. The Van der Waals interaction between rotating spherical particles [15] motivates

the investigation of the interaction between non-spherical rotating nanoparticles, with the possibility of a rotation-tunable superradianting emission. Furthermore, the calculations presented in chapter 3 consider only the electric dipole. The inclusion of the magnetic dipole of the nanoparticle can shed light on the role of the magnetic field in photon emission by metals. The spherical waves formalism allows for the inclusion of higher multipole moments of the nanoparticle and therefore can be employed for bigger particles in the Mie regime. The formalism developed in chapter 2 for the calculation of the force can be applied to other polarizable objects, enabling the exploration of quantum vacuum analogs of noninertial effects with macroscopic bodies.

In a field with many interesting results, this thesis brought new effects regarding the influence of relative rotations on the interaction of nanoparticles with the quantum vacuum and with atoms. This work is of experimental and theoretical relevance, as many experiments investigate phenomena related to the results presented here, and the methods developed by this thesis could be adapted to other quantum effects with rotating particles, therefore pushing the borders of our knowledge of dynamical quantum vacuum effects.

> *"The game of science is, in principle, without end. He who decides one day that scientific statements do not call for any further test, and that they can be regarded as finally verified, retires from the game."*
>
> — Karl Popper

# Bibliography

[1] Matos, G. C., Souza, R. d. M. e., Neto, P. A. M. & Impens, F. Quantum vacuum sagnac effect. *Physical Review Letters* **127**, 270401 (2021). xiv, xv, 15, 27, 73

[2] Ahn, J. *et al.* Optically levitated nanodumbbell torsion balance and ghz nanomechanical rotor. *Physical review letters* **121**, 033603 (2018). xv, 2, 14, 31, 37, 38

[3] Casimir, H. B. & Polder, D. The influence of retardation on the london-van der waals forces. *Physical Review* **73**, 360 (1948). 1, 4

[4] Casimir, H. B. On the attraction between two perfectly conducting plates. In *Proc. Kon. Ned. Akad. Wet.*, vol. 51, 793 (1948). 1

[5] Cougo-Pinto, M. V., Farina, C. & Tort, A. O efeito casimir. *Revista Brasileira de Ensino de Física* **22**, 122–132 (2000). 1

[6] Lamoreaux, S. K. Demonstration of the casimir force in the 0.6 to 6 $\mu$ m range. *Physical Review Letters* **78**, 5 (1997). 1

[7] Dalvit, D., Milonni, P., Roberts, D. & Da Rosa, F. *Casimir physics*, vol. 834 (Springer, 2011). 1

[8] Woods, L. M. *et al.* Materials perspective on casimir and van der waals interactions. *Reviews of Modern Physics* **88**, 045003 (2016). 1

[9] Xu, Z., Jacob, Z. & Li, T. Enhancement of rotational vacuum friction by surface photon tunneling. *Nanophotonics* **10**, 537–543 (2020). 1, 2, 31, 32, 43

[10] Lu, B.-S. The casimir effect in topological matter. *Universe* **7**, 237 (2021). 1

[11] Milton, K. A. *State Of The Quantum Vacuum, The: Casimir Physics In The 2020's* (World Scientific, 2022). 1

[12] Nakata, K. & Suzuki, K. Magnonic casimir effect in ferrimagnets. *Physical Review Letters* **130**, 096702 (2023). 1

[13] Schmidt, F. *et al.* Tunable critical casimir forces counteract casimir–lifshitz attraction. *Nature Physics* **19**, 271–278 (2023). 1

[14] Zhang, Y. *et al.* Magnetic-field tuning of the casimir force. *Nature Physics* **20**, 1282–1287 (2024). 1

[15] Amaral, H., Abrantes, P., Impens, F., Neto, P. & Souza, R. Tailoring the van der waals interaction with rotation. *arXiv preprint arXiv:2505.12177* (2025). 1, 48

[16] Milton, K. A., Høye, J. S. & Brevik, I. The reality of casimir friction. *Symmetry* **8**, 29 (2016). 1

[17] Reiche, D., Intravaia, F. & Busch, K. Wading through the void: Exploring quantum friction and nonequilibrium fluctuations. *APL Photonics* **7** (2022). 1

[18] Dodonov, V. Current status of the dynamical casimir effect. *Physica Scripta* **82**, 038105 (2010). 1, 31

[19] Dodonov, V. Fifty years of the dynamical casimir effect. *Physics* **2**, 67–104 (2020). 1, 31

[20] Dodonov, V. V. Dynamical casimir effect: 55 years later. *Physics* **7**, 10 (2025). 1, 31

[21] Dalvit, D. A., Neto, P. A. M. & Mazzitelli, F. D. Fluctuations, dissipation and the dynamical casimir effect. In *Casimir Physics*, 419–457 (Springer, 2011). 1, 31

[22] Pendry, J. B. Quantum friction–fact or fiction? *New Journal of Physics* **12**, 033028 (2010). 1

[23] Scheel, S. & Buhmann, S. Y. Casimir-polder forces on moving atoms. *Physical Review A—Atomic, Molecular, and Optical Physics* **80**, 042902 (2009). 1, 4

[24] Pieplow, G. & Henkel, C. Fully covariant radiation force on a polarizable particle. *New Journal of Physics* **15**, 023027 (2013). 1

[25] Donaire, M. & Lambrecht, A. Velocity-dependent dipole forces on an excited atom. *Physical Review A* **93**, 022701 (2016). 1

[26] Reiche, D., Intravaia, F., Hsiang, J.-T., Busch, K. & Hu, B.-L. Nonequilibrium thermodynamics of quantum friction. *Physical Review A* **102**, 050203 (2020). 1

[27] Farías, M. B., Lombardo, F. C., Soba, A., Villar, P. I. & Decca, R. S. Towards detecting traces of non-contact quantum friction in the corrections of the accumulated geometric phase. *npj Quantum Information* **6**, 25 (2020). 1, 3

[28] Fosco, C. D., Lombardo, F. C. & Mazzitelli, F. D. Motion-induced radiation due to an atom in the presence of a graphene plane. *Universe* **7**, 158 (2021). 1

[29] Lombardo, F. C., Decca, R. S., Viotti, L. & Villar, P. I. Detectable signature of quantum friction on a sliding particle in vacuum. *Advanced Quantum Technologies* **4**, 2000155 (2021). 1, 3, 8

[30] Guo, X., Milton, K. A., Kennedy, G. & Pourtolami, N. Quantum friction in the presence of a perfectly conducting plate. *Physical Review A* **107**, 062812 (2023). 1

[31] Kavokine, N., Bocquet, M.-L. & Bocquet, L. Fluctuation-induced quantum friction in nanoscale water flows. *Nature* **602**, 84–90 (2022). 1

[32] Oelschläger, M., Reiche, D., Egerland, C., Busch, K. & Intravaia, F. Electromagnetic viscosity in complex structured environments: From blackbody to quantum friction. *Physical Review A* **106**, 052205 (2022). 1

[33] Souza, R. d. M. e., Impens, F. & Neto, P. A. M. Microscopic dynamical casimir effect. *Physical Review A* **97**, 032514 (2018). 2, 37

[34] Lo, L. & Law, C. Quantum radiation from a shaken two-level atom in vacuum. *Physical Review A* **98**, 063807 (2018). 2

[35] Farías, M. B., Fosco, C. D., Lombardo, F. C. & Mazzitelli, F. D. Motion induced radiation and quantum friction for a moving atom. *Physical Review D* **100**, 036013 (2019). 2

[36] Dolan, B. P., Hunter-McCabe, A. & Twamley, J. Shaking photons from the vacuum: acceleration radiation from vibrating atoms. *New Journal of Physics* **22**, 033026 (2020). 2

[37] Agustí, A., García-Álvarez, L., Solano, E. & Sabín, C. Qubit motion as a microscopic model for the dynamical casimir effect. *Physical Review A* **103**, 062201 (2021). 2

[38] Ferreri, A., Pfeifer, H., Wilhelm, F. K., Hofferberth, S. & Bruschi, D. E. Interplay between optomechanics and the dynamical casimir effect. *Physical Review A* **106**, 033502 (2022). 2

[39] Alonso, L., Matos, G. C., Impens, F., Maia Neto, P. A. & de Melo e Souza, R. Multipole approach to the dynamical casimir effect with finite-size scatterers. *Entropy* **26**, 251 (2024). 2, 37

[40] de Oliveira, G. & Céleri, L. C. Thermodynamic entropy production in the dynamical casimir effect. *Physical Review A* **109**, 012807 (2024). 2

[41] Jiang, T.-h. & Jing, J. Realizing a mechanical dynamical casimir effect with a low-frequency oscillator. *Physical Review A* **111**, 022811 (2025). 2

[42] Yu, R. & Fan, S. Near-field dynamical casimir effect. *Physical Review Letters* **135**, 116901 (2025). 2

[43] Stickler, B. A., Hornberger, K. & Kim, M. Quantum rotations of nanoparticles. *Nature Reviews Physics* **3**, 589–597 (2021). 2

[44] Ahn, J. *et al.* Ultrasensitive torque detection with an optically levitated nanorotor. *Nature Nanotechnology* **15**, 89–93 (2020). 2, 13, 14, 18, 26, 31, 37, 44, 71

[45] Ju, P. *et al.* Near-field ghz rotation and sensing with an optically levitated nanodumbbell. *Nano letters* **23**, 10157–10163 (2023). 2, 31, 48, 71

[46] Reimann, R. *et al.* Ghz rotation of an optically trapped nanoparticle in vacuum. *Physical review letters* **121**, 033602 (2018). 2, 14

[47] Schuck, M., Steinert, D., Nussbaumer, T. & Kolar, J. W. Ultrafast rotation of magnetically levitated macroscopic steel spheres. *Science advances* **4**, e1701519 (2018). 2, 44

[48] Jin, Y. *et al.* 6 ghz hyperfast rotation of an optically levitated nanoparticle in vacuum. *Photonics Research* **9**, 1344–1350 (2021). 2, 31, 37, 71

[49] Delić, U. *et al.* Cooling of a levitated nanoparticle to the motional quantum ground state. *Science* **367**, 892–895 (2020). 2

[50] Manjavacas, A. & García de Abajo, F. J. Thermal and vacuum friction acting on rotating particles. *Physical Review A—Atomic, Molecular, and Optical Physics* **82**, 063827 (2010). 2, 15, 18, 31, 34, 68, 71

[51] Manjavacas, A. & García de Abajo, F. J. Vacuum friction in rotating particles. *Physical review letters* **105**, 113601 (2010). 2, 15, 31

[52] Manjavacas, A., Rodríguez-Fortuño, F. J., de Abajo, F. J. G. & Zayats, A. V. Lateral Casimir force on a rotating particle near a planar surface. *Physical Review Letters* **118**, 133605 (2017). 2

[53] Zhao, R., Manjavacas, A., García de Abajo, F. J. & Pendry, J. Rotational quantum friction. *Physical review letters* **109**, 123604 (2012). 2, 31

[54] Impens, F., Ttira, C. C., Behunin, R. O. & Neto, P. A. M. Dynamical local and nonlocal casimir atomic phases. *Physical Review A* **89**, 022516 (2014). 2, 5, 6, 11, 16, 73

[55] Sagnac, G. Sur la preuve de la réalité de l'éther lumineux par l'expérience de l'interférographe tournant. *Comptes Rendus de l'Academie des Sciences* **157**, 1410–1413 (1913). 3, 13

[56] Intravaia, F., Henkel, C. & Antezza, M. Fluctuation-induced forces between atoms and surfaces: The casimir–polder interaction. In *Casimir Physics*, 345–391 (Springer, 2011). 4, 29, 66

[57] Cronin, A. D. & Perreault, J. D. Phasor analysis of atom diffraction from a rotated material grating. *Physical Review A—Atomic, Molecular, and Optical Physics* **70**, 043607 (2004). 4, 9, 23, 25, 26

[58] Perreault, J. D. & Cronin, A. D. Observation of atom wave phase shifts induced by van der waals atom-surface interactions. *Physical review letters* **95**, 133201 (2005). 4, 9

[59] Lepoutre, S. *et al.* Atom interferometry measurement of the atom-surface van der waals interaction. *The European Physical Journal D* **62**, 309–325 (2011). 4, 23, 25, 26, 27

[60] Garcion, C. *et al.* Intermediate-range casimir-polder interaction probed by high-order slow atom diffraction. *Physical Review Letters* **127**, 170402 (2021). 4

[61] Lecoffre, J. *et al.* Measurement of casimir-polder interaction for slow atoms through a material grating. *Physical Review Research* **7**, 013232 (2025). 4

[62] Nemirovsky, J., Weill, R., Meltzer, I. & Sagi, Y. Atomic interferometer based on optical tweezers. *Physical Review Research* **5**, 043300 (2023). 5

[63] Narducci, F. A., Black, A. T. & Burke, J. H. Advances toward fieldable atom interferometers. *Advances in Physics: X* **7**, 1946426 (2022). 5

[64] Ryu, C. & Boshier, M. G. Integrated coherent matter wave circuits. *New Journal of Physics* **17**, 092002 (2015). 5, 18, 22

[65] Amico, L. *et al.* Colloquium: Atomtronic circuits: From many-body physics to quantum technologies. *Reviews of Modern Physics* **94**, 041001 (2022). 5

[66] Stern, A., Aharonov, Y. & Imry, Y. Phase uncertainty and loss of interference: A general picture. *Physical Review A* **41**, 3436 (1990). 6

[67] Gundhi, A. Decoherence due to the casimir effect? *Physical Review D* **110**, 116001 (2024). 8

[68] Dalvit, D. A. & Neto, P. A. M. Decoherence via the dynamical casimir effect. *Physical review letters* **84**, 798 (2000). 8

[69] Viotti, L., Belén Farías, M., Villar, P. I. & Lombardo, F. C. Thermal corrections to quantum friction and decoherence: A closed-time-path approach to atom-surface interaction. *Physical Review D* **99**, 105005 (2019). 8

[70] Impens, F., Behunin, R. O., Ttira, C. C. & Neto, P. A. M. Non-local double-path casimir phase in atom interferometers. *Europhysics letters* **101**, 60006 (2013). 12

[71] Yu, Y. *et al.* Mems gyroscopes based on acoustic sagnac effect. *Micromachines* **8**, 2 (2016). 13

[72] Bordé, C. J. Atomic interferometry with internal state labelling. *Physics letters A* **140**, 10–12 (1989). 13

[73] Gustavson, T. L., Bouyer, P. & Kasevich, M. A. Precision rotation measurements with an atom interferometer gyroscope. *Physical review letters* **78**, 2046 (1997). 13

[74] Lenef, A. *et al.* Rotation sensing with an atom interferometer. *Physical review letters* **78**, 760 (1997). 13

[75] Savoie, D. *et al.* Interleaved atom interferometry for high-sensitivity inertial measurements. *Science advances* **4**, eaau7948 (2018). 13

[76] Gautier, R. *et al.* Accurate measurement of the sagnac effect for matter waves. *Science Advances* **8**, eabn8009 (2022). 13

[77] d'Armagnac de Castanet, Q. *et al.* Atom interferometry at arbitrary orientations and rotation rates. *Nature Communications* **15**, 6406 (2024). 13

[78] Canuel, B. *et al.* Six-axis inertial sensor using cold-atom interferometry. *Physical review letters* **97**, 010402 (2006). 13

[79] Cronin, A. D., Schmiedmayer, J. & Pritchard, D. E. Optics and interferometry with atoms and molecules. *Reviews of Modern Physics* **81**, 1051–1129 (2009). 13

[80] Moan, E. *et al.* Quantum rotation sensing with dual sagnac interferometers in an atom-optical waveguide. *Physical review letters* **124**, 120403 (2020). 13, 22

[81] Geiger, R., Landragin, A., Merlet, S. & Pereira Dos Santos, F. High-accuracy inertial measurements with cold-atom sensors. *AVS Quantum Science* **2** (2020). 13, 14, 27

[82] Schubert, C. *et al.* Multi-loop atomic sagnac interferometry. *Scientific Reports* **11**, 16121 (2021). 13

[83] Kumiya, T., Akentyev, A. S., Mori, Y., Ichimura, J. & Morinaga, A. Milliradian-phase-resolution atom interferometer with transparent electrodes for measurement of the röntgen phase. *Physical Review A* **93**, 023637 (2016). 14

[84] Neto, P. M. & Machado, L. Quantum radiation generated by a moving mirror in free space. *Physical Review A* **54**, 3420 (1996). 14

[85] Woods, L. M., Krüger, M. & Dodonov, V. V. Perspective on some recent and future developments in casimir interactions. *Applied Sciences* **11**, 293 (2020). 14, 31, 32

[86] Dalvit, D. A. & Kort-Kamp, W. J. Shaping dynamical casimir photons. *Universe* **7**, 189 (2021). 14, 32

[87] Shapere, A. & Wilczek, F. *Geometric phases in physics*, vol. 5 (World scientific, 1989). 14, 21

[88] Aharonov, Y. & Bohm, D. Further considerations on electromagnetic potentials in the quantum theory. *Physical Review* **123**, 1511 (1961). 14

[89] Barton, G. The quantum radiation from mirrors moving sideways. *annals of physics* **245**, 361–388 (1996). 15

[90] Heitler, W. *The quantum theory of radiation* (Courier Corporation, 1984). 17

[91] Cohen-Tannoudji, C., Dupont-Roc, J. & Grynberg, G. *Photons and atoms-introduction to quantum electrodynamics* (1997). 17, 33, 66, 76

[92] Blaber, M. G., Arnold, M. D. & Ford, M. J. Search for the ideal plasmonic nanoshell: the effects of surface scattering and alternatives to gold and silver. *The Journal of Physical Chemistry C* **113**, 3041–3045 (2009). 18, 24

[93] Post, E. J. Sagnac effect. *Reviews of Modern Physics* **39**, 475 (1967). 20

[94] Dalibard, J., Gerbier, F., Juzeliūnas, G. & Öhberg, P. Colloquium: Artificial gauge potentials for neutral atoms. *Reviews of Modern Physics* **83**, 1523–1543 (2011). 20, 28

[95] Schweikhard, V., Coddington, I., Engels, P., Mogendorff, V. P. & Cornell, E. A. Rapidly rotating bose-einstein condensates in and near the lowest landau level. *Physical review letters* **92**, 040404 (2004). 20, 28

[96] Impens, F., e Souza, R. d. M., Matos, G. C. & Neto, P. A. M. Dynamical casimir effects with atoms: From the emission of photon pairs to geometric phases. *Europhysics Letters* **138**, 30001 (2022). 20

[97] Paiva, I. L., Lenny, R. & Cohen, E. Geometric phases and the sagnac effect: foundational aspects and sensing applications. *Advanced Quantum Technologies* **5**, 2100121 (2022). 20, 21, 28

[98] Aharonov, Y. & Bohm, D. Significance of electromagnetic potentials in the quantum theory. *Physical review* **115**, 485 (1959). 20, 28

[99] Berry, M. V. Quantal phase factors accompanying adiabatic changes. *Proceedings of the Royal Society of London. A. Mathematical and Physical Sciences* **392**, 45–57 (1984). 21

[100] Xiao, D., Chang, M.-C. & Niu, Q. Berry phase effects on electronic properties. *Reviews of modern physics* **82**, 1959–2007 (2010). 21

[101] Hasman, E., Kleiner, V., Biener, G. & Niv, A. Polarization dependent focusing lens by use of quantized pancharatnam–berry phase diffractive optics. *Applied physics letters* **82**, 328–330 (2003). 21

[102] Bliokh, K. Y. Geometrical optics of beams with vortices: Berry phase and orbital angular momentum hall effect. *Physical Review Letters* **97**, 043901 (2006). 21

[103] Band, Y., Kuzmenko, I. & Avishai, Y. Geometric phases in optics: Polarization of light propagating in helical optical fibers. *Physical Review A* **111**, 033530 (2025). 21

[104] Baer, M. *Beyond Born-Oppenheimer: electronic nonadiabatic coupling terms and conical intersections* (John Wiley & Sons, 2006). 21

[105] Resta, R. Manifestations of berry's phase in molecules and condensed matter. *Journal of Physics: Condensed Matter* **12**, R107–R143 (2000). 21

[106] Hsin, P.-S., Kapustin, A. & Thorngren, R. Berry phase in quantum field theory: Diabolical points and boundary phenomena. *Physical Review B* **102**, 245113 (2020). 21

[107] Cirilo-Lombardo, D. J. & Sanchez, N. G. Entanglement and generalized berry geometrical phases in quantum gravity. *Symmetry* **16**, 1026 (2024). 21

[108] Lepoutre, S. *et al.* Dispersive atom interferometry phase shifts due to atom-surface interactions. *Europhysics Letters* **88**, 20002 (2009). 23, 25, 26

[109] Scholl, J. A., Koh, A. L. & Dionne, J. A. Quantum plasmon resonances of individual metallic nanoparticles. *Nature* **483**, 421–427 (2012). 24

[110] Holmgren, W. F., Revelle, M. C., Lonij, V. P. & Cronin, A. D. Absolute and ratio measurements of the polarizability of na, k, and rb with an atom interferometer. *Physical Review A—Atomic, Molecular, and Optical Physics* **81**, 053607 (2010). 24

[111] Timp, G. *et al.* Using light as a lens for submicron, neutral-atom lithography. *Physical review letters* **69**, 1636 (1992). 26

[112] Richberg, R. & Martin, A. Focusing of bragg-outcoupled paraxial atom lasers. *Physical Review A* **104**, 033314 (2021). 26

[113] Salvi, L., Poli, N., Vuletić, V. & Tino, G. M. Squeezing on momentum states for atom interferometry. *Physical review letters* **120**, 033601 (2018). 27

[114] Jackson, J. D. *Classical electrodynamics* (Wiley, New York, NY, 1975). 28

[115] Blūms, V. *et al.* A single-atom 3d sub-attonewton force sensor. *Science advances* **4**, eaao4453 (2018). 30

[116] Sciama, D. W. On the origin of inertia. *Monthly Notices of the Royal Astronomical Society* **113**, 34–42 (1953). 30

[117] Moore, G. T. Quantum theory of the electromagnetic field in a variable-length one-dimensional cavity. *Journal of mathematical physics* **11**, 2679–2691 (1970). 31

[118] Khosravi, F., Sun, W., Khandekar, C., Li, T. & Jacob, Z. Giant enhancement of vacuum friction in spinning yig nanospheres. *New Journal of Physics* **26**, 053006 (2024). 31

[119] Maghrebi, M. F., Jaffe, R. L. & Kardar, M. Spontaneous emission by rotating objects: A scattering approach. *Phys. Rev. Lett.* **108**, 230403 (2012). 31

[120] Dodonov, V., Klimov, A. & Man'ko, V. Generation of squeezed states in a resonator with a moving wall. *Physics Letters A* **149**, 225–228 (1990). 32

[121] Dodonov, V. & Klimov, A. Long-time asymptotics of a quantized electromagnetic field in a resonator with oscillating boundary. *Physics Letters A* **167**, 309–313 (1992). 32

[122] Maia Neto, P. A. & Machado, L. A. S. Quantum radiation generated by a moving mirror in free space. *Physical Review A* **54**, 3420–3427 (1996). 32, 33, 37

[123] Maghrebi, M. F., Golestanian, R. & Kardar, M. Scattering approach to the dynamical Casimir effect. *Phys. Rev. D* **87**, 025016 (2013). 32

[124] Turky, A. O., Rashad, M. M., Kandil, A. E.-H. T. & Bechelany, M. Tuning the optical, electrical and magnetic properties of $Ba_{0.5}Sr_{0.5}Ti_xM_{1-x}O_3$ (BST) nanopowders. *Phys. Chem. Chem. Phys.* **17**, 12553 (2015). 32

[125] Turky, A. O., Rashad, M. M. & Bechelany, M. Tailoring optical and dielectric properties of $Ba_{0.5}Sr_{0.5}TiO_3$ powders synthesized using citrate precursor route. *Materials & Design* **90**, 54 (2016). 32

[126] Berestetski, V., Lifshitz, E. M. & Pitaevskii, L. *Relativistic Quantum Theory Volume 1* (Pergamon, 1971). 33

[127] Maia Neto, P. A. Vacuum radiation pressure on moving mirrors. *J. Phys. A: Math. Gen.* **27**, 2167 (1994). 37

[128] Ford, L. H. & Vilenkin, A. Quantum radiation by moving mirrors. *Phys. Rev. D* **25**, 2569–2575 (1982). 37

[129] Maia Neto, P. A. & Reynaud, S. Dissipative force on a sphere moving in vacuum. *Phys. Rev. A* **47**, 1639–1646 (1993). 37

[130] Felderhof, B. & Palaniappan, D. Longitudinal and transverse polarizability of the conducting double sphere. *Journal of applied physics* **88**, 4947–4952 (2000). 37

[131] Lide, D. (ed.) *CRC Handbook of Chemistry and Physics, 85th ed.* (PCRC Press, Boca Raton, 2004). 38

[132] Landau, L. D. & Lífshíts, E. M. *Electrodynamics of continuous media* (Pergamon press Oxford, 1946). 38

[133] Bell, R. & Rupprecht, G. Elastic constants of strontium titanate. *Physical Review* **129**, 90 (1963). 45

[134] Kubo, R. The fluctuation-dissipation theorem. *Reports on progress in physics* **29**, 255 (1966). 64

[135] Santos, A. S. *et al.* Time-dependent effective hamiltonians for light–matter interactions. *Entropy* **26**, 527 (2024). 66

[136] Berestetskii, V. B., Pitaevskii, L. P. & Lifshitz, E. M. *Quantum Electrodynamics: Volume 4*, vol. 4 (Elsevier, 2012). 76

# Appendix A

# Linear Response Theory

The inclusion of an interaction term in the hamiltonian of the system changes the temporal evolution of the system's observables. This appendix presents the temporal evolution of operators in first order of perturbation theory in terms of susceptibilities, a formalism known as linear response theory [134]. The results are then applied for an atom interacting with the quantum electric field.

## A.1 Response functions

Suppose a quantum system with a stationary hamiltonian $H_0$. At $t = 0$ it is introduced a time dependent perturbation $V(t)$ in the form

$$V(t) = -f(t)M, \tag{A.1}$$

with $M$ being an operator of the system and $f$ a given function of time. In order to determine the time evolution of the average of an observable $N$ in first order in $f$, we use the Liouville equation to obtain the system's density matrix $\rho(t)$, namely

$$i\hbar\frac{d\rho}{dt}(t) = [H_0 + V(t), \rho(t)]. \tag{A.2}$$

All the operators in Eq. A.2 are in the Schrödinger picture. To further explore the effect of $V(t)$ in the dynamic of the system, we rewrite the Liouville equation in the interaction picture:

$$i\hbar\frac{d\tilde{\rho}}{dt}(t) = [\tilde{V}(t), \tilde{\rho}(t)], \tag{A.3}$$

where $\tilde{A}(t) := e^{\frac{i}{\hbar}H_0 t} A e^{-\frac{i}{\hbar}H_0 t}$ is the operator in the interaction picture. The first order solution of Eq. A.3 is

$$\tilde{\rho}(t) = \rho_0 - \frac{i}{\hbar}\int_0^t f(t')[\tilde{M}(t'), \rho_0]\, dt' + \mathcal{O}(f^2), \tag{A.4}$$

where $\rho_0$ is the density matrix for the unperturbed system. We then switch back to Schrödinger picture, finding

$$\rho(t) = \rho_0 + \frac{i}{\hbar}\int_{-\infty}^t f(t')\theta(t-t')[\tilde{M}(t'-t), \rho_0]\, dt'. \tag{A.5}$$

The Heaviside step function is included to ensure causality: a perturbation at instant $t'$ has its effects on the system at a later instant $t$.

The average of an operator $N$ as a function of time can be obtained explicitly with the density matrix

$$\langle N \rangle (t) = \mathrm{Tr}(\rho(t)N). \tag{A.6}$$

Therefore, using Eq. A.5 we have

$$\langle N \rangle_{(t)} = \langle N \rangle_0 + \int_{-\infty}^t f(t')\chi_{NM}(t-t')dt'. \tag{A.7}$$

The function $\chi_{NM}(\tau)$ is defined by

$$\chi_{NM}(\tau) := \frac{i}{\hbar}\theta(\tau)\left\langle [N, \tilde{M}(-\tau)] \right\rangle_{eq}. \tag{A.8}$$

With $\langle .. \rangle_0$ being the average with $\rho_0$. $\chi_{NM}(\tau)$ is the response function or susceptibility of $N$. It determines the induction of the physical quantity related to $N$ arising from the application of $M$.

## A.2 Atomic electric dipole and electric field susceptibilities

Within the dipole approximation, an atom interacting with the quantum electric field has two outcomes: the field induces a dipole on the atom, and the atomic fluctuating

dipole produces an electric field. In this section, we express these quantities in terms of response functions.

We start from the dipolar interaction hamiltonian

$$V = -\mathbf{d}(t) \cdot \mathbf{E}(\mathbf{r}', t), \tag{A.9}$$

where $\mathbf{r}'$ is the atomic position. Given that the hamiltonian is bilinear, it is possible to separate the dipole and field into free-evolving and induced contributions [56]

$$\begin{aligned} \mathbf{d}(t) &= \tilde{\mathbf{d}}(t) + \mathbf{d}^{ind}(t) \\ \mathbf{E}(\mathbf{r}, t) &= \tilde{\mathbf{E}}(\mathbf{r}, t) + \mathbf{E}^{ind}(\mathbf{r}, t). \end{aligned} \tag{A.10}$$

The temporal evolution of Eq. A.7 allows the identification of the induced observables with the susceptibilities:

$$\langle \mathbf{E}^{ind}(\mathbf{r}, t) \rangle = \frac{i}{\hbar} \int_{-\infty}^{t} d\tau \theta(\tau) \langle [\tilde{\mathbf{E}}(\mathbf{r}, t), \tilde{\mathbf{E}}(\mathbf{r}', t-\tau)] \rangle \cdot \langle \tilde{\mathbf{d}}(t-\tau) \rangle \tag{A.11}$$

$$\langle \mathbf{d}^{ind}(t) \rangle = \frac{i}{\hbar} \int_{-\infty}^{t} d\tau \theta(\tau) \langle [\tilde{\mathbf{d}}(t), \tilde{\mathbf{d}}(t-\tau)] \rangle \cdot \langle \tilde{\mathbf{E}}(\mathbf{r}', t-\tau) \rangle . \tag{A.12}$$

Eq. A.11 represents the field produced by an electric dipole, and therefore the susceptibility of the field is the retarded Green function from electrodynamics, i.e., the propagator of for a dipole field (see Appendix A of Ref. [135] for a demonstration). Therefore, the definition is

$$G^R_{lm}(\mathbf{r}, t; \mathbf{r}', t') := \frac{i}{\hbar} \theta(t-t') \langle [E_l(\mathbf{r}, t), E_m(\mathbf{r}', t')] \rangle . \tag{A.13}$$

Note that the average of the commutator is a complex function that does not depend on the field state, due to the electric field expression in terms of bosonic operators. For a dipole in free space at position $\mathbf{r}'$, the retarded Green function is symmetric by spatial and temporal translations [91], and thus

$$G^R_{lm}(\mathbf{r}, t; \mathbf{r}', t') = G^R_{lm}(|\mathbf{r} - \mathbf{r}'|, t - t'). \tag{A.14}$$

The response function for the atomic dipole in Eq. A.12 is the polarizability, which gives the induced dipole under the application of an electric field. Contrary to the retarded Green's function, the polarizability does depend on the atom state $|a\rangle$, typically

written on the basis of eigenstates of the atom hamiltonian. The definition of the atomic polarizability is

$$\alpha^A_{a\,lm}(t,t') := \frac{i}{\hbar}\theta(t-t')\,\langle a|[d_l(t), d_m(t')]|a\rangle\,. \tag{A.15}$$

In this thesis, the polarizability is with respect to the atom ground state for all discussions, and therefore we omit the state dependency.

Taking the Fourier transform of equations A.11 and A.12 we have a clearer relation between the induced operators and the response functions:

$$\mathbf{d}^{ind}(\omega) = \boldsymbol{\alpha}^A(\omega)\cdot\tilde{\mathbf{E}}(\mathbf{r}',\omega) \tag{A.16}$$

$$\mathbf{E}^{ind}(\mathbf{r},\omega) = \mathbf{G}^R(\mathbf{r},\mathbf{r}',\omega)\cdot\tilde{\mathbf{d}}(\omega). \tag{A.17}$$

Equation A.17 is exact, consequence of of the linearity of Maxwell equations. On the other hand, Eq. A.16 is an approximation for weak fields. In Fourier space, the explicit expression for the retarded Green's function is

$$G_{lm}(\mathbf{r},\mathbf{r}',\omega) = \frac{e^{ikR}}{4\pi\epsilon_0 R^3}\left[(k^2R^2+ikR-1)\delta_{lm} - (k^2R^2+3ikR-3)\frac{R_l R_m}{R^2}\right], \tag{A.18}$$

where $\mathbf{R} := \mathbf{r}-\mathbf{r}'$ and $k = \omega/c$. For a two level atom, the ground state polarizability in Fourier space is the known expression

$$\alpha^A_{lm}(\omega) = \frac{\alpha^A_0\omega_0}{\omega_0^2-\omega^2}\delta_{lm}, \tag{A.19}$$

with $\alpha^A_0$ being the static polarizability and $\omega_0$ the transition frequency.

# Appendix B

# Polarizability of a Rotating Particle

A neutral polarizable particle in the presence of an electric field can have an induced dipole. The constitutive relation involves its polarizability tensor $\boldsymbol{\alpha}$

$$\mathbf{d}(\omega) = \boldsymbol{\alpha}(\omega) \cdot \mathbf{E}(\omega) \tag{B.1}$$

The rotation of a polarizable particle changes the constitutive relation, producing rotational Doppler shifts. This appendix reproduces the semiclassical derivation of the effective polarizability for a rotating spherical object presented by Manjavacas & de Abajo in Ref. [50]. The same method is employed to derive the induced dipole of a spinning non-spherical object.

## B.1 Polarizability for a rotating spherical particle

Eq. B.1 is defined for the rest frame of the object. In order to establish an analog relation, we write the rest frame field and dipole in terms of the vectors in the laboratory frame, and then apply in Eq. B.1.

The transformation between frames is done by a rotation matrix $\mathcal{R}$. A vector $\mathbf{v}'(t)$ in the rotating frame is mapped to the laboratory frame vector $\mathbf{v}(t)$ by the relation

$$\mathbf{v}(t) = \mathcal{R}\mathbf{v}'(t). \tag{B.2}$$

If the angular velocity is $\mathbf{\Omega} = \Omega\hat{\mathbf{z}}$, the matrix is

$$\mathcal{R}_{(\Omega t)} = \begin{pmatrix} \cos\Omega t & -\sin\Omega t & 0 \\ \sin\Omega t & \cos\Omega t & 0 \\ 0 & 0 & 1 \end{pmatrix}. \tag{B.3}$$

Therefore, the electric dipole vector $\mathbf{d}(\omega)$ is

$$\begin{aligned} d_x(\omega) &= \frac{1}{2}[d'_x(\omega_+) + d'_x(\omega_-) + id'_y(\omega_+) - id'_y(\omega_-)] \\ d_y(\omega) &= \frac{1}{2}[-id'_x(\omega_+) + id'_x(\omega_-) + d'_y(\omega_+) + d'_y(\omega_-)], \end{aligned} \tag{B.4}$$

with $\omega_\pm := \omega \pm \Omega$. As expected, the z-component is not affected by rotation. Eq. B.4 is the Fourier transform of the relation B.2 for the dipole in the time domain $\mathbf{d}(t)$.

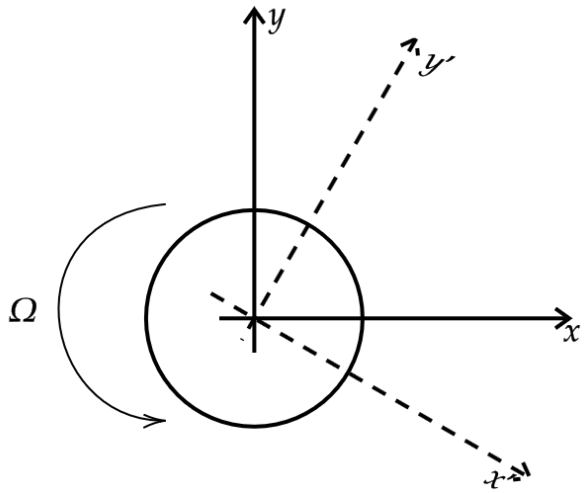


Figure B.1: Schematization of the rotating frame ($x'y'$) and laboratory frame ($xy$) for a spinning spherical object.

For a spherical particle at rest, the polarizability tensor is a multiple of the identity:

$$\boldsymbol{\alpha}^0(\omega) = \tilde{\alpha}(\omega)\mathbb{1} \tag{B.5}$$

Thus, $\mathbf{d}'(\omega) = \tilde{\alpha}(\omega)\mathbf{E}'(\omega)$. Eq. B.4 then becomes

$$\begin{aligned} d_x &= \frac{1}{2}[\tilde{\alpha}(\omega_+)E'_x(\omega_+) + \tilde{\alpha}(\omega_-)E'_x(\omega_-) + i\tilde{\alpha}(\omega_+)E'_y(\omega_+) - i\tilde{\alpha}(\omega_-)E'_y(\omega_-)] \\ d_y &= \frac{1}{2}[-i\tilde{\alpha}(\omega_+)E'_x(\omega_+) + i\tilde{\alpha}(\omega_-)E'_x(\omega_-) + \tilde{\alpha}(\omega_+)E'_y(\omega_+) + \tilde{\alpha}(\omega_-)E'_y(\omega_-)]. \end{aligned} \tag{B.6}$$

Equation B.2 can also be used to obtain the electric field in the laboratory frame. In the frequency domain, we have the relation

$$\begin{aligned} E_x(\omega) + iE_y(\omega) &= E'_x(\omega_+) + iE'_y(\omega_+) \\ E_x(\omega) - iE_y(\omega) &= E'_x(\omega_-) - iE'_y(\omega_-). \end{aligned} \tag{B.7}$$

Eq. B.7 is analogous to the raising and lowering operators of the quantum harmonic oscillator. By substituting the above equation into Eq. B.6, we have an expression relating both the dipole and electric field in the lab frame. Hence, it is immediate to obtain the effective polarizability for a rotating spherical particle

$$\boldsymbol{\alpha}^{\Omega}(\omega) = \begin{pmatrix} \alpha_{xx}(\omega) & \alpha_{xy}(\omega) & 0 \\ \alpha_{yx}(\omega) & \alpha_{yy}(\omega) & 0 \\ 0 & 0 & \tilde{\alpha}(\omega) \end{pmatrix}, \tag{B.8}$$

with

$$\begin{aligned} \alpha_{xx}(\omega) = \alpha_{yy}(\omega) &:= \frac{\tilde{\alpha}(\omega_+) + \tilde{\alpha}(\omega_-)}{2} \\ \alpha_{xy}(\omega) = -\alpha_{yx}(\omega) &:= \frac{i[\tilde{\alpha}(\omega_+) - \tilde{\alpha}(\omega_-)]}{2}. \end{aligned} \tag{B.9}$$

Note that the rotation preserves the reality property of the effective polarizability,

$$\boldsymbol{\alpha}^{\Omega}(-\omega) = (\boldsymbol{\alpha}^{\Omega}(\omega))^*. \tag{B.10}$$

Naturally, if $\Omega \to 0$ we recover Eq. B.5. The rotation breaks isotropy, and even for a sphere the effective polarizability has off-diagonal elements. If the rotation angular frequency is much lower than the typical resonant frequencies of the material, the polarizability can be expanded in first order in $\Omega$

$$\boldsymbol{\alpha}^{\Omega}(\omega) = \begin{pmatrix} \tilde{\alpha}(\omega) & i\Omega\tilde{\alpha}'(\omega) & 0 \\ -i\Omega\tilde{\alpha}'(\omega) & \tilde{\alpha}(\omega) & 0 \\ 0 & 0 & \tilde{\alpha}(\omega) \end{pmatrix}, \tag{B.11}$$

where the primes indicate derivative with respect to $\omega$. From Eq. B.11 one can see the dependence on the material's dispersion in order for the effects of rotation to manifest in the electric response. The above equation can be generalized to any angular velocity vector $\boldsymbol{\Omega}$:

$$\alpha^{\boldsymbol{\Omega}}_{lm}(\omega) = \alpha^{0}_{lm}(\omega) + i\tilde{\alpha}'(\omega)\epsilon_{lmn}\Omega_n. \tag{B.12}$$

This method can also be applied for a non-spherical object, as long as the angular velocity is parallel to the particle symmetry axis [50].

## B.2 Polarizability for a non-spherical rotating particle

The results from the previous section do not apply for a nonspherical particle rotating with angular velocity perpendicular to its symmetry axis. This case (which is of experimental relevance [44, 45, 48]) is derived in this section.

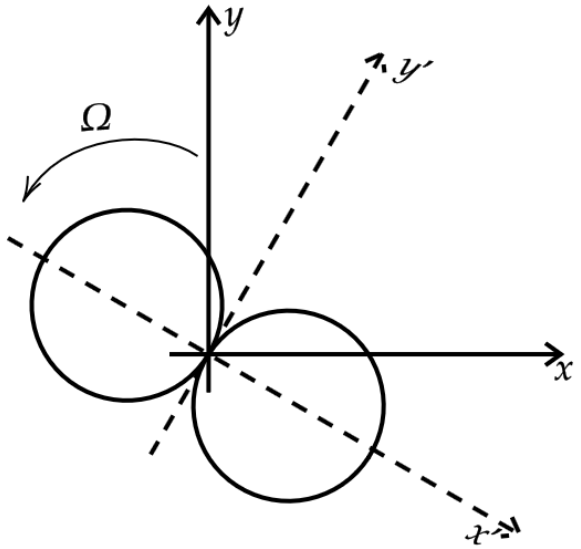


Figure B.2: Schematization of the rotating frame ($x'y'$) and laboratory frame ($xy$) for a spinning dumbbell-shaped object.

For a particle whose shape is given by a solid of revolution, with $x'$ being its symmetry axis, the polarizability at rest is

$$\boldsymbol{\alpha}^0(\omega) = \begin{pmatrix} \alpha_\parallel & 0 & 0 \\ 0 & \alpha_\perp & 0 \\ 0 & 0 & \alpha_\perp \end{pmatrix}. \tag{B.13}$$

Given the rotation around the $z$-axis, we can use the rotation matrix defined in Eq. B.3 to write the dipole moment in the lab frame. It is convenient to define the functions

$$\begin{aligned} S &= \frac{\alpha_\parallel(\omega) + \alpha_\perp(\omega)}{2} \\ \Delta &= \frac{\alpha_\parallel(\omega) - \alpha_\perp(\omega)}{2}. \end{aligned} \tag{B.14}$$

Hence

$$\begin{aligned} d_x(\omega) &= \frac{1}{2}[S^+(E_x(\omega)+iE_y(\omega)) + S^-(E_x(\omega)-iE_y(\omega))+ \\ &+ \Delta^+(E'_x(\omega_+) - iE'_y(\omega_+)) + \Delta^-(E'_x(\omega_-) + iE'_y(\omega_-))] \\ d_y(\omega) &= \frac{1}{2}[S^+(-iE_x(\omega)+E_y(\omega)) + S^-(iE_x(\omega)+E_y(\omega))- \\ &- \Delta^+(iE'_x(\omega_+) + E'_y(\omega_+)) + \Delta^-(iE'_x(\omega_-) - E'_y(\omega_-))], \end{aligned} \tag{B.15}$$

where $S^\pm = S(\omega_\pm)$ and $\Delta^\pm = \Delta(\omega_\pm)$. We have used Eq. B.7. The same equation can be used iteratively (since it is valid for all $\omega$) to write

$$\begin{aligned} E_x(\omega-2\Omega) + iE_y(\omega-2\Omega) &= E'_x(\omega-\Omega) + iE'_y(\omega-\Omega) \\ E_x(\omega+2\Omega) - iE_y(\omega+2\Omega) &= E'_x(\omega+\Omega) - iE'_y(\omega+\Omega), \end{aligned} \tag{B.16}$$

Substituting Eq. B.16 into Eq. B.15 results in an analog constitutive relation for the dipole induced by a field:

$$\mathbf{d}(\omega) = \boldsymbol{\alpha}_0(\omega)\mathbf{E}(\omega) + \boldsymbol{\alpha}_+(\omega)\mathbf{E}(\omega+2\Omega) + \boldsymbol{\alpha}_-(\omega)\mathbf{E}(\omega-2\Omega), \tag{B.17}$$

on which

$$\begin{aligned} \boldsymbol{\alpha}_0(\omega) &:= \begin{pmatrix} \frac{1}{2}(S^+ + S^-) & \frac{i}{2}(S^+ - S^-) & 0 \\ \frac{-i}{2}(S^+ - S^-) & \frac{1}{2}(S^+ + S^-) & 0 \\ 0 & 0 & \alpha_\perp(\omega) \end{pmatrix} \\ \boldsymbol{\alpha}_\pm(\omega) &:= \frac{\Delta(\omega \pm \Omega)}{2} \begin{pmatrix} 1 & \mp i & 0 \\ \mp i & -1 & 0 \\ 0 & 0 & 0 \end{pmatrix}. \end{aligned} \tag{B.18}$$

Here, the dipole of frequency $\omega$ is not produced only by the field mode with the same frequency, as in the spherical case, but there is also a contribution from field modes of frequencies shifted by $2\Omega$. This is a consequence of the continuous time translation symmetry breaking due to the rotation, which gives rise to a discrete time translation of half of the period, and therefore the frequency modulation of $2\Omega$. Moreover, this case does not relies on the dispersion of the material to manifest effects of the spinning in the polarizability.

# Appendix C

# Quantum Vacuum Sagnac Phase as a Berry Phase

A Berry phase is a geometric phase produced on the system eigenstates during an adiabatic evolution. In this appendix, we present the demonstration by F. Impens [1] that the QVSP is a Berry phase.

The starting point is to write the phase along a path $\mathbf{r}_k$ as a second order term in the Dyson series [54] following the formalism developed in chapter 1:

$$\phi_k = \frac{i}{2\hbar^2}\int_{-T/2}^{T/2} dt \int_{-T/2}^{t} dt' \left(\langle g,0|\, \tilde{H}_{int}(\mathbf{r}_k(t),t)\tilde{H}_{int}(\mathbf{r}_k(t'),t')\,|g,0\rangle - c.c.\right). \tag{C.1}$$

Here, $|g,0\rangle = |g\rangle_A \otimes |0\rangle_F$ is the initial state prepared at the lowest energy state of the system, i.e., the 2-level atom at its ground state and the field at the vacuum. Making the same approximations for the atomic motion when deriving the QVSP, the motional phase is written as

$$\phi_k^{\Omega} = \frac{i}{2\hbar^2}\int_{-T/2}^{T/2} dt \mathbf{v}_k(t)\cdot\int_{-T/2}^{t+T/2} d\tau\tau \left(\langle g,0|\, \tilde{H}_{int}(\mathbf{r}_k(t),t)\nabla\tilde{H}_{int}(\mathbf{r}_k(t),t-\tau)\,|g,0\rangle - c.c.\right), \tag{C.2}$$

with $\tau = t - t'$. Switching the representation of the operators to the Schrödinger picture and taking the one photon states $|e,n\rangle = |e\rangle_A\,|1_n\rangle_F$ as the basis, which are eigenstates of

the free hamiltonian of the system $H_0$, the closure relation can be employed to obtain

$$\phi_k^{\Omega} = \frac{i}{2\hbar^2}\int_{\mathcal{P}_k} d\mathbf{r}\cdot\left(\sum_{n\neq 0}\langle g,0|\, H_{int}(\mathbf{r})\,|e,n\rangle\,\langle e,n|\,\nabla H_{int}(\mathbf{r})\,|g,0\rangle\int_0^{\infty} d\tau\,\tau e^{-i(\omega_n-\omega_0)} - c.c.\right). \tag{C.3}$$

The summation over $n$ is a sum over polarizations and wavevectors of the field modes. The frequencies $\omega_n$ and $\omega_0$ are the eigenenergies divided by $\hbar$ of $H_0$ associated to eigenstates $|e,n\rangle$ and $|g,0\rangle$.The temporal integral becomes geometric along the path $\mathcal{P}_k$ using $d\mathbf{r} = dt\mathbf{v}_k$. The sum over $n$ excludes the ground state since $\langle g,0|\, H_{int}(\mathbf{r})\,|g,0\rangle = 0$. The integration in $\tau$ can be carried resulting in

$$\phi_k^{\Omega} = \frac{i}{2\hbar^2}\int_{\mathcal{P}_k} d\mathbf{r}\cdot\left(\sum_{n\neq 0}\frac{\langle g,0|\, H_{int}(\mathbf{r})\,|e,n\rangle\,\langle e,n|\,\nabla H_{int}(\mathbf{r})\,|g,0\rangle}{(\omega_n-\omega_0)^2} - c.c.\right). \tag{C.4}$$

The expression of the motional phase Eq. (C.4) can also be obtained by integrating the corresponding Berry connection and is therefore equal to the Berry phase. Let $|\psi_0(\mathbf{r})\rangle$ be the ground state of the atom+field system taking the interaction as non-perturbative. Consistently with the previous derivation, the Berry phase must be calculated within second order in perturbation of the interaction hamiltonian. Hence, using the same basis as before, the ground state in terms of the unperturbed stated is

$$\begin{aligned}|\psi_0(\mathbf{r})\rangle = |g,0\rangle &+ \sum_{n\neq 0}\frac{\langle e,n|\, H_{int}(\mathbf{r})\,|g,0\rangle}{\hbar(\omega_n-\omega_0)}\,|e,n\rangle - \frac{1}{2}\sum_{n\neq 0}\frac{|\,\langle e,n|\, H_{int}(\mathbf{r})\,|g,0\rangle\,|^2}{\hbar^2(\omega_n-\omega_0)^2}\,|g,0\rangle \\ &+ \sum_{n\neq 0,n'\neq n}\frac{\langle e,n|\, H_{int}(\mathbf{r})\,|e,n'\rangle\,\langle e,n'|\, H_{int}(\mathbf{r})\,|g,0\rangle}{\hbar^2(\omega_0-\omega_n)(\omega_n-\omega_n')}\,|e,n\rangle \\ &- \sum_{n\neq 0}\frac{\langle e,n|\, V(\mathbf{r})\,|g,0\rangle\,\langle g,0|\, H_{int}(\mathbf{r})\,|g,0\rangle}{\hbar^2(\omega_n-\omega_0)^2}\,|e,n\rangle + \mathcal{O}(H_{int}^3).\end{aligned} \tag{C.5}$$

Since the interaction Hamiltonian is linear in the dipole operator, the terms $\langle e,n|\, H_{int}(\mathbf{r})\,|e,n'\rangle$ and $\langle g,0|\, H_{int}(\mathbf{r})\,|g,0\rangle$ are zero given the diagonal terms of the dipole operator vanish regardless of the field state. Thus

$$\begin{aligned}|\nabla\psi_0(\mathbf{r})\rangle &= \sum_{n\neq 0}\frac{\langle e,n|\nabla H_{int}(\mathbf{r})|g,0\rangle}{\hbar(\omega_n-\omega_0)}\,|e,n\rangle \\ &- \frac{1}{2}\sum_{n\neq 0}\left(\frac{\langle g,0|\nabla H_{int}(\mathbf{r})|e,n\rangle\,\langle e,n|H_{int}(\mathbf{r})|g,0\rangle}{\hbar^2(\omega_n-\omega_0)^2} + c.c.\right)|g,0\rangle + \mathcal{O}(H_{int}^3).\end{aligned} \tag{C.6}$$

Hence, the Berry connection (integrand in Eq. (2.15)) is

$$i\left\langle \psi_0(\mathbf{r})|\nabla\psi_0(\mathbf{r})\right\rangle = \frac{i}{2\hbar^2}\sum_{n\neq 0}\left(\frac{\left\langle g,0\right| H_{int}(\mathbf{r})\left|e,n\right\rangle \left\langle e,n\right|\nabla H_{int}(\mathbf{r})\left|g,0\right\rangle}{(\omega_n-\omega_0)^2}+c.c.\right)+\mathcal{O}(H_{int}^3) \tag{C.7}$$

Integrating Eq.(C.7) along the path $\mathcal{P}_k$ results in phase given by Eq. (C.4), completing the proof that the QVSP is a Berry phase.

# Appendix D

# Quantum Electromagnetic Field With Spherical Waves

This appendix presents expressions for the electric and magnetic fields operators on the spherical wave basis and some important related results as well. The complete quantization of the electromagnetic field with multipole waves can be found in Refs. [91, 136]. The results presented here are from Ref. [91].

The electric field operator in frequency domain expressed as a sum of multipole wave is

$$\mathbf{E}(\mathbf{r},\omega) = i\mathcal{E}(\omega)\sum_{j=1}^{\infty}\sum_{m=-j}^{j}\sum_{\lambda=\mathrm{E,M}} a_{jm\lambda}(\omega)\theta(\omega)\mathbf{I}_{jm\lambda}(\mathbf{r},\omega) - a^{\dagger}_{jm\lambda}(-\omega)\theta(-\omega)\mathbf{I}^{*}_{jm\lambda}(\mathbf{r},\omega), \quad \text{(D.1)}$$

where $\mathcal{E}(\omega) = \sqrt{\frac{\hbar\omega}{2\epsilon_0 c}}$ is the mode amplitude. The quantum numbers $j, m$ specify the order of the multipole. $\lambda$ is the polarization, indicating if the multipole is electric or magnetic. Given that multipole waves are also eigenstates of angular momentum, $j$ is also related to the eigenvalues $j(j+1)\hbar^2$ of the squared total total angular momentum operator $J^2$, while $m\hbar$ is the eigenvalue of the z-component of the angular momentum. $\mathbf{I}_{jm\lambda}(\mathbf{r},\omega)$ is the vector spherical harmonic of the mode, which carries the spatial dependence of the field. By the canonical quantization process, the operator $a_{jm\lambda}(\omega)$ and $a^{\dagger}_{jm\lambda}(\omega)$ obey the commutation rule

$$[a^{\mathrm{in}}_{jm\lambda}(\omega), a^{\mathrm{in}}_{j'm'\lambda'}(\omega')^{\dagger}] = \delta(\omega-\omega')\delta_{jj'}\delta_{mm'}\delta_{\lambda\lambda'}. \quad \text{(D.2)}$$

The magnetic field is

$$c\mathbf{B}(\mathbf{r},\omega) = i\mathcal{E}(\omega)\sum_{j=1}^{\infty}\sum_{m=-j}^{j}(a_{jmE}(\omega)\mathbf{I}_{jmB}(\mathbf{r},\omega) - a_{jmB}(\omega)\mathbf{I}_{jmE}(\mathbf{r},\omega))\theta(\omega) \\ - (a^{\dagger}_{jmE}(-\omega)\mathbf{I}^{*}_{jmB}(\mathbf{r},\omega) - a^{\dagger}_{jmB}(-\omega)\mathbf{I}^{*}_{jmE}(\mathbf{r},\omega))\theta(-\omega). \tag{D.3}$$

The explicit expression for the vector spherical harmonic depends on the polarization. For magnetic multipoles, we have

$$\mathbf{I}_{jmB}(\mathbf{r},\omega) = 4\pi\frac{\omega}{c}i^{j}\mathscr{J}_{j}(\omega r/c)\mathbf{X}_{jm}(\hat{\mathbf{r}}), \quad \mathbf{X}_{jm}(\hat{\mathbf{r}}) := \frac{1}{\sqrt{j(j+1)}}\hat{\mathbf{r}}\times\nabla_{\hat{\mathbf{r}}}Y_{jm}(\hat{\mathbf{r}}). \tag{D.4}$$

Here, $\nabla_{\hat{\mathbf{r}}}$ denotes the gradient acting only on the angular coordinates, and $\mathscr{J}_{j}(\omega r/c)$ is the $j$ spherical Bessel function of the first kind. The electric multipoles vector spherical harmonics are given by

$$\mathbf{I}_{jmE}(\mathbf{r},\omega) = \frac{4\pi i^{j-1}}{r}\left[\sqrt{j(j+1)}\,\mathscr{J}_{j}(\omega r/c)\mathbf{N}_{jm}(\hat{\mathbf{r}}) + \frac{d}{dx}(x\,\mathscr{J}_{j}(x))\Big|_{x=\omega r/c}\mathbf{Z}_{jm}(\hat{\mathbf{r}})\right], \tag{D.5}$$

where

$$\mathbf{N}_{jm}(\hat{\mathbf{r}}) := \hat{\mathbf{r}}Y_{jm}(\hat{\mathbf{r}}) \\ \mathbf{Z}_{jm}(\hat{\mathbf{r}}) := \frac{1}{\sqrt{j(j+1)}}\nabla_{\hat{\mathbf{r}}}Y_{jm}(\hat{\mathbf{r}}). \tag{D.6}$$

An important limit is the radiation zone regime, which occurs when $\omega r/c \gg 1$. In that case, we can use the asymptotic form of the spherical Bessel functions

$$\mathscr{J}_{j}(\omega r/c) \approx \frac{c}{\omega r}\sin(\omega r/c - j\pi/2), \tag{D.7}$$

to obtain the following expressions for the vector spherical harmonics

$$\mathbf{I}_{jmE}(\mathbf{r}) = 4\pi i^{J-1}\frac{\cos(\frac{\omega r}{c} - j\frac{\pi}{2})}{r}\mathbf{Z}_{jm}(\hat{\mathbf{r}}) \\ \mathbf{I}_{jmB}(\mathbf{r}) = 4\pi i^{J}\frac{\sin(\frac{\omega r}{c} - j\frac{\pi}{2})}{r}\mathbf{X}_{jm}(\hat{\mathbf{r}}). \tag{D.8}$$